

# Extremely Massive Quasars are not Good Proxies for Dense Environments Compared to Massive Galaxies: Environments of Extremely Massive Quasars and Galaxies

YONGMIN YOON,<sup>1</sup> MYUNGSHIN IM,<sup>1</sup> MINHEE HYUN,<sup>1</sup> HYUNSUNG DAVID JUN,<sup>2</sup> NARAE HWANG,<sup>3</sup> MINJIN KIM,<sup>3,4</sup> AND  
BYEONG-GON PARK<sup>3</sup>

<sup>1</sup>*Center for the Exploration of the Origin of the Universe (CEOU), Astronomy Program, Department of Physics and Astronomy, Seoul National University, 1 Gwanak-ro, Gwanak-gu, Seoul, 151-742, Republic of Korea*

<sup>2</sup>*School of Physics, Korea Institute for Advanced Study, 85 Hoegiro, Dongdaemun-gu, Seoul 02455, Republic of Korea*

<sup>3</sup>*Korea Astronomy and Space Science Institute, 776 Daedeokdae-ro, Yuseong-gu, Daejeon 34055, Republic of Korea*

<sup>4</sup>*Department of Astronomy and Atmospheric Sciences, Kyungpook National University, Daegu 702-701, Republic of Korea*

## ABSTRACT

Black hole mass scaling relations suggest that extremely massive black holes (EMBHs) with  $M_{\text{BH}} \gtrsim 10^{9.4} M_{\odot}$  are found in the most massive galaxies with  $M_{\text{star}} \gtrsim 10^{11.6} M_{\odot}$ , which are commonly found in dense environments, like galaxy clusters. Therefore, one can expect that there is a close connection between active EMBHs and dense environments. Here, we study the environments of 9461 galaxies and 2943 quasars at  $0.24 \leq z \leq 0.40$ , among which 52 are extremely massive quasars with  $\log(M_{\text{BH}}/M_{\odot}) \geq 9.4$ , using Sloan Digital Sky Survey and MMT Hectospec data. We find that, on average, both massive quasars and massive galaxies reside in environments more than  $\sim 2$  times as dense as those of their less massive counterparts with  $\log(M_{\text{BH}}/M_{\odot}) \lesssim 9.0$ . However, massive quasars reside in environments about half as dense as inactive galaxies with  $\log(M_{\text{BH}}/M_{\odot}) \geq 9.4$ , and only about one third of massive quasars are found in galaxy clusters, while about two thirds of massive galaxies reside in such clusters. This indicates that massive galaxies are a much better signpost for galaxy clusters than massive quasars. The prevalence of massive quasars in moderate to low density environments is puzzling, considering that several simulation results show that these quasars appear to prefer dense environments. Several possible reasons for this discrepancy are discussed, although further investigation is needed to obtain a definite explanation.

*Keywords:* galaxies: active — galaxies: evolution — galaxies: nuclei — quasars: supermassive black holes

## 1. INTRODUCTION

Extremely massive black holes (EMBHs) are the most massive black holes (BHs) in the universe with BH masses of  $\sim 10^{10} M_{\odot}$ . EMBHs were discovered in nearby early-type galaxies (McConnell et al. 2011; van den Bosch et al. 2012), in line with previous results that suggest the existence of very massive BHs in quasars (e.g., Netzer 2003; Vestergaard et al. 2008; Wu et al. 2015; Kim et al. 2018).

BH mass scaling relations in the local universe suggest that EMBHs reside in very massive, passively evolving early-type galaxies, with stellar masses larger than  $\sim 10^{11.6} M_{\odot}$  according to an extension of the currently

known BH mass scaling relation (e.g., Kormendy & Ho 2013). Such massive galaxies are usually found in highly dense environments (Eisenstein et al. 2005; Zehavi et al. 2005; Coil et al. 2006) and massive dark-matter halos with  $M_{\text{halo}} \gtrsim 10^{14} M_{\odot}$  (Behroozi et al. 2010; Leauthaud et al. 2012; Yang et al. 2012). Therefore, EMBHs are expected to reside in highly dense environments, like galaxy clusters.

EMBHs are also identified in active galactic nuclei (AGNs; Shen & Liu 2012; Jun et al. 2015, 2017). Active EMBHs are among the brightest objects in the universe, and this opens up the possibility of using them as signposts to identify galaxy clusters at low to high redshifts that are useful for constraining cosmological models and galaxy evolution models (e.g. Wen & Han 2011; Strazzullo et al. 2013; Kang & Im 2015; Lee et al. 2015; Kim et al. 2016). In several previous studies, quasars with

supermassive black holes (SMBHs) of  $\sim 10^9 M_\odot$  and at  $z \lesssim 2$  are found to reside in environments denser than less massive SMBHs, although the trend is not very strong (Shen et al. 2009; Komiya et al. 2013; Zhang et al. 2013; Krolewski & Eisenstein 2015; Krumpel et al. 2015; Shirasaki et al. 2016; Song et al. 2016). So, it is still an open question whether active EMBHs reside in environments that are considerably denser than those of inactive EMBHs.

Galaxy formation simulations suggest that active EMBHs tend to reside in dense environments, at least at low redshifts ( $z \lesssim 1$ ), but not quite so at higher redshifts. Fanidakis et al. (2013b) examined the environments of luminous quasars ( $\log(L_{\text{bol}}/\text{erg s}^{-1}) \gtrsim 45$ ) using the GALFORM simulation data, where the formation and evolution of galaxies and BHs are coupled within the hierarchical clustering of dark-matter distribution (Fanidakis et al. 2011, 2012). In the simulation, AGN activity is fueled by two modes: one is the “starburst” mode, where gas-rich merger or disk instability causes cold-gas accretion onto BHs, and the other is the “hot-halo” mode, where the cooling of hot gas in massive dark-matter halos is responsible for AGN activity. Their simulation shows that luminous quasars (not necessarily massive ones) at  $z \sim 0$  can be either hot-halo-mode quasars in massive halos ( $> 10^{14} M_\odot$ ) or starburst-mode quasars in halos with  $M_{\text{halo}} \sim 10^{12} M_\odot$ . They also identified that luminous quasars with massive host galaxies — i.e., galaxies with EMBHs — are mostly in hot-halo mode, so their results indicate that the majority of active EMBHs are quasars in hot-halo mode and in massive halos at low redshifts. At higher redshifts, the starburst mode becomes the prevailing mode of quasar activity, and many EMBHs seem to reside at lower-mass halos, not even in the location where they would grow into superclusters at  $z \sim 0$  (Fanidakis et al. 2013b). Observational results appear to agree with such conclusions for quasars at  $z \gtrsim 4$  (e.g., Kim et al. 2009; Bañados et al. 2013; Husband et al. 2013; Simpson et al. 2014; Uchiyama et al. 2018).

So far, studies of the environments of active EMBHs are very scarce due to their low number density, but with the availability of large-area surveys it has become possible to undertake a comprehensive study of the environment of rare objects like EMBHs. In this paper, we study the environments of active and inactive SMBHs at  $0.24 \leq z \leq 0.40$ , with a special focus on the environments of EMBHs. By doing so, we identify active EMBHs in dense environments and examine how common such cases are. In addition, we compare the environments of active EMBHs with those of inactive EMBHs in galaxies whose bulge masses match the BH masses of the

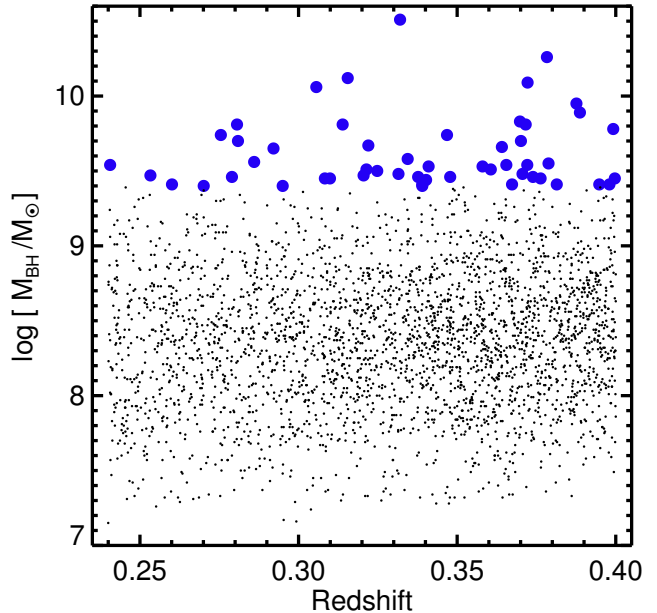


**Figure 1.** Fifty-two massive quasars among the full 2943-quasar sample in the redshift–BH mass plane. The blue circles are the 52 massive quasars with  $\log(M_{\text{BH}}/M_\odot) \geq 9.4$ .

active EMBHs through a scaling relation. We discuss why the environments of massive quasars and those of mass-matched galaxies are different, suggesting possible reasons associated with quasar-triggering mechanisms, the BH mass scaling relation, and uncertainty in BH mass measurements. We also discuss if active/inactive EMBHs can be good signposts for galaxy clusters out to a moderate redshift ( $z \lesssim 2$ ), and investigate whether the result agrees with simulations.

Throughout this paper, we use  $H_0 = 70 \text{ km s}^{-1} \text{ Mpc}^{-1}$ ,  $\Omega_\Lambda = 0.7$ , and  $\Omega_m = 0.3$  as cosmological parameters, which are supported by previous observations (e.g., Im et al. 1997; Planck Collaboration et al. 2016). We use transverse comoving distances to convert angles in the sky into transverse distances in this paper.

## 2. SAMPLE

### 2.1. Quasar Sample

The quasars we use here were chosen from the quasar catalog of Shen et al. (2011, hereafter S11). We used quasars with spectroscopic redshifts in the redshift range of  $0.24 \leq z \leq 0.40$ . The upper limit of the range was chosen to include H $\alpha$  lines (at least partially) in the spectra, and the lower limit was chosen to limit the quasar sample to a narrow redshift range to avoid complexities in the analysis due to quasar evolution, such as in

**Table 1.** Properties of Extremely Massive Quasars

Name	Redshift	$\log(L_{5100}/\text{erg s}^{-1})$	$\text{FWHM}_{\text{H}\beta}$ (km s $^{-1}$ )	$\log(M_{\text{BH}}/M_{\odot})$	$\delta_{0.5 \text{ Mpc}}$	$\delta_{7\text{th}}$	DPE
J004319.73+005115.4	0.3083	44.65 ± 0.006	12788 ± 381	9.45 ± 0.03	2.3	0.3	Y
J010900.36+151217.5	0.3788	44.99 ± 0.004	11761 ± 521	9.55 ± 0.04	4.3	4.4	Y
J013253.32−095239.4	0.2601	44.08 ± 0.014	17075 ± 422	9.41 ± 0.02	6.5	4.1	Y
J031332.88−063157.9	0.3887	44.35 ± 0.003	25328 ± 2913	9.89 ± 0.10	0.9	0.7	Y
J032559.97+000800.7	0.3606	44.76 ± 0.006	12891 ± 246	9.51 ± 0.02	0.7	2.2	N
J075403.60+481428.0	0.2755	44.81 ± 0.004	16242 ± 219	9.74 ± 0.01	−1.0	0.1	Y
J075407.95+431610.6	0.3478	44.94 ± 0.004	10945 ± 154	9.46 ± 0.01	−0.1	−0.3	Y
J080644.42+484149.2	0.3701	44.92 ± 0.001	14618 ± 829	9.70 ± 0.05	3.3	3.1	N
J085039.95+543753.3	0.3673	44.58 ± 0.006	12714 ± 620	9.41 ± 0.04	−0.1	0.2	N
J092158.92+034235.7	0.3248	44.26 ± 0.009	17004 ± 1435	9.50 ± 0.07	4.0	4.3	N
J095746.83+303024.2	0.3344	44.23 ± 0.001	18938 ± 907	9.58 ± 0.04	3.7	4.6	N
J100027.44+025951.2	0.3390	44.47 ± 0.006	13384 ± 567	9.40 ± 0.04	0.8	0.6	Y
J100726.10+124856.2	0.2406	45.41 ± 0.001	9208 ± 580	9.54 ± 0.05	1.4	1.7	N
J101226.85+261327.2	0.3783	44.51 ± 0.003	35297 ± 2097	10.26 ± 0.05	1.7	−0.2	Y
J102738.53+605016.4	0.3320	44.86 ± 0.004	38343 ± 1853	10.51 ± 0.04	0.9	0.6	Y
J102817.67+211507.4	0.3655	44.18 ± 0.008	18726 ± 7675	9.54 ± 0.36	−0.1	−0.1	N
J104709.83+130454.6	0.3997	44.69 ± 0.006	12468 ± 495	9.45 ± 0.03	0.0	−0.1	Y
J104820.12+302627.5	0.3876	44.87 ± 0.001	20046 ± 1575	9.95 ± 0.07	0.9	−0.1	N
J105224.07+373004.5	0.3739	44.41 ± 0.008	14788 ± 654	9.46 ± 0.04	3.4	2.3	Y
J111121.71+482045.9	0.2809	44.52 ± 0.001	18460 ± 7795	9.70 ± 0.37	0.2	−0.3	Y
J111724.57+153800.5	0.3698	45.24 ± 0.020	14118 ± 551	9.83 ± 0.04	1.6	1.8	N
J111800.12+233651.5	0.3814	44.49 ± 0.001	13422 ± 717	9.41 ± 0.05	2.6	−0.0	N
J114631.67+274624.1	0.3139	44.70 ± 0.004	18776 ± 8713	9.81 ± 0.40	0.1	0.0	Y
J115431.49+121427.4	0.2701	44.44 ± 0.003	13598 ± 845	9.40 ± 0.05	2.7	1.1	Y
J120924.07+103612.0	0.3948	45.36 ± 0.005	8162 ± 234	9.41 ± 0.03	−0.0	−0.4	N
J123215.16+132032.7	0.2860	44.55 ± 0.004	15502 ± 551	9.56 ± 0.03	6.2	6.5	Y
J123807.76+532555.9	0.3468	44.78 ± 0.001	16587 ± 598	9.74 ± 0.03	2.5	0.3	Y
J123852.17+231638.2	0.3410	44.32 ± 0.006	16858 ± 1070	9.53 ± 0.06	1.7	−0.0	Y
J125105.07+380744.3	0.3056	44.12 ± 0.001	35297 ± 1908	10.06 ± 0.05	3.4	−0.3	Y
J125327.70+145456.0	0.2533	44.45 ± 0.004	14684 ± 263	9.47 ± 0.02	−1.0	−0.5	Y
J125809.31+351943.0	0.3099	44.33 ± 0.001	15366 ± 1301	9.45 ± 0.07	1.2	0.1	Y
J132404.20+433407.1	0.3377	44.38 ± 0.008	15132 ± 1121	9.46 ± 0.06	−1.0	−0.3	Y
J133433.24−013825.3	0.2921	44.30 ± 0.010	19717 ± 2731	9.65 ± 0.12	0.2	0.8	Y
J133957.99+613933.5	0.3721	44.59 ± 0.007	14679 ± 774	9.54 ± 0.05	0.7	1.3	Y
J135354.89+134228.5	0.3722	44.66 ± 0.007	26450 ± 4218	10.09 ± 0.14	2.5	3.9	N
J140019.26+631427.0	0.3315	44.66 ± 0.005	13189 ± 508	9.48 ± 0.03	−0.0	−0.2	Y
J140506.21+171707.9	0.3402	44.71 ± 0.007	12181 ± 479	9.44 ± 0.03	−0.1	0.0	N
J141213.61+021202.1	0.2950	44.29 ± 0.008	14826 ± 2499	9.40 ± 0.15	0.2	0.0	Y
J142735.60+263214.5	0.3641	45.15 ± 0.018	12200 ± 459	9.66 ± 0.03	−0.1	0.3	N
J145331.47+264946.7	0.2790	44.36 ± 0.007	15309 ± 2331	9.46 ± 0.13	0.2	4.3	Y
J150019.08+000249.0	0.3763	44.33 ± 0.010	15357 ± 1466	9.45 ± 0.08	−0.1	−0.2	N
J150752.66+133844.5	0.3220	44.79 ± 0.001	15303 ± 417	9.67 ± 0.02	1.0	1.5	N
J153142.08+132834.5	0.3980	44.32 ± 0.002	14834 ± 1847	9.41 ± 0.11	5.0	3.3	N
J154019.56−020505.4	0.3205	45.08 ± 0.034	10228 ± 634	9.47 ± 0.06	0.0	−0.5	Y
J154426.06+000923.5	0.2806	44.12 ± 0.006	26359 ± 7058	9.81 ± 0.23	3.9	2.5	Y
J155846.72+223549.6	0.3992	44.84 ± 0.004	16893 ± 622	9.78 ± 0.03	10.2	19.1	Y
J160053.61+024500.2	0.3706	44.46 ± 0.006	14880 ± 4118	9.48 ± 0.24	−0.1	0.4	N
J160534.13+230950.0	0.3155	44.23 ± 0.004	35297 ± 3020	10.12 ± 0.07	1.1	1.0	N
J160737.16+455235.2	0.3214	44.35 ± 0.007	16420 ± 390	9.51 ± 0.02	−1.0	−0.4	Y
J163856.53+433512.5	0.3390	44.61 ± 0.001	12552 ± 545	9.41 ± 0.04	0.8	0.4	N
J165118.62+400124.8	0.3580	44.94 ± 0.000	11933 ± 249	9.53 ± 0.02	−1.0	−0.6	N
J170441.38+604430.5	0.3716	45.79 ± 0.003	10031 ± 419	9.81 ± 0.04	−0.1	−0.1	N

NOTE— $\delta_{0.5 \text{ Mpc}}$  is the overdensities around the quasars measured in an aperture with a radius of 0.5 Mpc, while  $\delta_{7\text{th}}$  is the overdensities around quasars measured in an aperture whose radius corresponds to the projected distance to the seventh nearest galaxy. Quasars with double-peaked broad H $\beta$  emission lines are marked as Y in DPE column. Otherwise, N is marked in that column (see Section 5.2.6 for classification of double-peaked broad H $\beta$  lines).

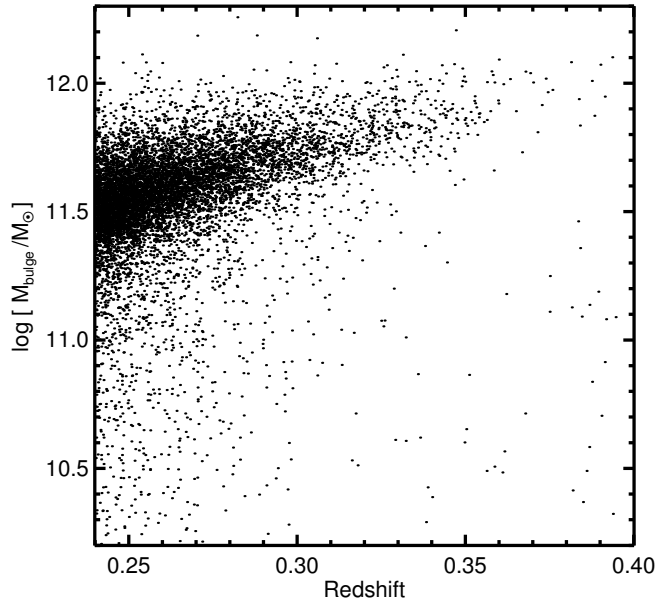


**Figure 2.** Galaxy sample in the redshift–bulge stellar mass plane. The bulge masses were used as proxies for BH masses in inactive galaxies.

the  $M_{\text{BH}}$ –host galaxy scaling relation.<sup>1</sup> The number of quasars in this redshift range is 4073.

Some quasars in the quasar catalog have very weak and quite broad  $\text{H}\beta$  lines on the continua. Visual inspection of such broad emission line spectra with a low signal-to-noise ratio ( $\text{S/N} < 8$ ) suggested that they could be spurious and the BH mass measurements could be erroneous. Therefore, we excluded quasars with such emission lines by imposing a criterion on the uncertainties in logarithmic broad  $\text{H}\beta$  line luminosities of less than or equal to 0.05, which corresponds to  $\text{S/N}$  higher than  $\sim 8$ . This selection criterion brings down the number of quasars to 2943.

Among this quasar sample, we defined quasars whose BH masses are larger than  $10^{9.4} M_{\odot}$  as massive quasars (active EMBHs). For these massive quasars, we adopted the masses of the SMBHs in the catalog of S11 measured by the method of the single-epoch measurement in Vestergaard & Peterson (2006) based on broad  $\text{H}\beta$  lines. The number of these massive quasars is 52. The properties of these quasars are summarized in Table 1. Figure 1 shows our sample of 52 massive quasars among the full 2943-quasar sample in the redshift–BH mass plane.

Considering that the automatic procedure of S11 may produce spurious results, we examined the reliability of

the BH mass measurements at the massive end by performing a full multicomponent fitting analysis for the spectra of the 52 massive quasars (Appendix A). We found that except for a few of the massive quasars,<sup>2</sup> the BH masses from S11 agree with our measurements within  $\sim 0.1$  dex. There would have been no meaningful change in the results of this paper whether we adopted S11’s or our measurements. Therefore, we used the BH masses presented by S11 for massive quasars for consistency with the analysis of the full 2943-quasar sample, in which the BH masses are from the S11 catalog.

We checked the consistency between the  $\text{H}\beta$ -based BH masses and the  $\text{H}\alpha$ -based BH masses for quasars at  $0.24 \leq z \leq 0.31$  (see Appendix B). Note that the upper limit in redshift is 0.31, because the  $\text{H}\alpha$  line fit window moves out of the spectral coverage beyond this redshift. We found that the two BH mass estimates agree with each other with an intrinsic scatter of 0.14 dex. As shown in Appendix B, we repeated the whole BH mass–overdensity correlation analyses shown below using  $\text{H}\alpha$ -based BH mass values, and the main results of this paper on the environment around massive quasars and massive inactive galaxies are similar to the  $\text{H}\beta$ -based results. Thus, we will present the results from the virial BH masses measured by broad  $\text{H}\beta$  lines. Note that the  $\text{H}\alpha$  lines at  $z > 0.31$ , although only partial profiles are available, were useful for checking the reliability of the broad  $\text{H}\beta$  line profile shapes.

## 2.2. Galaxy Sample (Inactive SMBHs)

To study the environment of inactive BHs, we used galaxies from the catalog of Mendel et al. (2014, hereafter M14), for which bulge masses were available. The availability of bulge masses allowed us to convert them to BH masses, and then construct BH mass-matched galaxy samples. The M14 catalog is based on the catalog of Simard et al. (2011), who fitted two-dimensional surface brightness profiles to derive structural parameters for 1,123,718 galaxies from Sloan Digital Sky Survey (SDSS) Data Release 7 (Abazajian et al. 2009). For the galaxies observed with spectroscopy, M14 derived the total, bulge, and disk stellar masses by the method of spectral energy distribution (SED) fitting. They used the initial mass function (IMF) of Chabrier (2003), the flexible stellar population synthesis model (Conroy et al. 2009), and the extinction law of Calzetti et al. (2000) for the SED fitting.

<sup>1</sup> We note that only 4 massive quasars are found at  $z < 0.24$ .

<sup>2</sup> We found nine quasars whose BH masses from S11 are larger than our estimates by more than 0.3 dex (see Appendix A).





completeness limit of  $\sim 90\%$  for detection and  $\sim 95\%$  for source classification for the SDSS data (Wang et al. 2013). As we shall show in Section 3, the photometric redshift accuracy is  $\Delta z/(1+z) \sim 0.028$  for the SDSS galaxies at  $m_r < 21$ , which is sufficient for investigating large-scale environments.

#### 2.4. MMT Hectospec Data

For three massive quasars,<sup>8</sup> we observed galaxies in the radius of  $\sim 0.5$  degrees from these quasars using the Hectospec on the MMT (Fabricant et al. 2008). The Hectospec is a spectrograph with 300 fibers with a  $1.5''$  aperture, and its wavelength coverage is from  $\sim 3700\text{\AA}$  to  $\sim 8500\text{\AA}$  with a spectral resolution of  $\sim 6.2\text{\AA}$  and a dispersion of  $1.2\text{\AA pixel}^{-1}$ . The targets for the observations were galaxies with  $m_r < 21$  and in the photometric redshift range of  $z_{\text{quasar}} - 0.1 \lesssim z \lesssim z_{\text{quasar}} + 0.1$ , where  $z_{\text{quasar}}$  is the spectroscopic redshift of the central quasar. We assigned some of the fibers to several spectrophotometric F-type standard stars for flux calibration, following the selection criteria in Shim et al. (2013). Several tens of fibers were assigned to blank sky areas for sky subtraction. The total exposure time was 1 hr per fiber configuration (split into three 20 minute exposures).

Data reduction was done by the HSRED package for Hectospec (Kochanek et al. 2012), performing bias and flat field correction, wavelength calibration, and sky subtraction. The extracted one-dimensional spectra were flux-calibrated using the observed F-type stars and the spectral models of F-type stars given by HSRED. For each F-type star, we matched the spectral models of F-type stars based on color values ( $g-r$  and  $r-i$ ) and found the best-matched spectral model.

Spectroscopic redshifts were measured by the IDL-based program SpecPro (Masters & Capak 2011). The redshifts were determined by cross-correlation between galaxy spectral templates with several absorption lines and/or emission lines and the observed spectra. To determine the redshifts, we used at least two spectral features, such as CaK, CaH, G-band, Mg I, or Na I for absorption lines and [O II], H $\beta$ , [O III], or H $\alpha$  lines for emission lines.

Among the 762 fibers assigned to the targets, 4.5% (34) are stars, while we could not detect redshifts for 8.8% (67) due to low S/N values. Overall, the redshift identification rate is 91.2%. Figure 3 shows examples of the Hectospec spectra. We present the measured red-

**Table 2.** Galaxies observed by the MMT Hectospec

R.A.	Decl.	Redshift	$m_r$	Redshift Measurement
239.20068	22.48715	0.2405	20.16	E
239.21014	22.46478	0.4779	19.67	A
239.21715	22.42390	0.3767	19.78	E
239.22235	22.58807	0.5238	20.88	E
239.22830	22.64405	0.3291	19.29	A
239.22941	22.54767	0.3708	19.15	A
239.24275	22.41755	0.3289	19.69	A,E

NOTE—In the last column, we mark “A” for objects whose redshifts were measured by templates with absorption lines, while “E” is marked for objects whose redshifts were measured by templates with emission lines. We mark “A,E” for objects whose redshifts were measured by templates with both absorption and emission lines. This table is available in its entirety in machine-readable form.

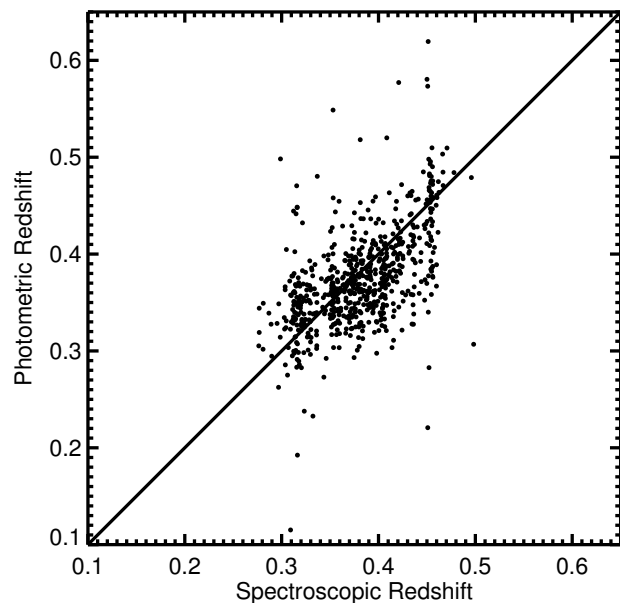


**Figure 4.** Comparison between the photometric redshifts and the spectroscopic redshifts of the MMT Hectospec data combined with the SDSS DR12 spectroscopic data. The galaxies with  $M_r^c < -19.8$  in the spectroscopic redshift range of  $z_{\text{quasar}} - 0.1 \leq z \leq z_{\text{quasar}} + 0.1$  were used. We find that the rms value of the difference between the photometric redshifts and the spectroscopic redshifts is  $dv \sim 8500\text{km s}^{-1}$  ( $\Delta z/(1+z) \sim 0.028$ ) except  $\sim 3\%$  outliers.

shifts from the Hectospec observations in Table 2.

### 3. ENVIRONMENT MEASUREMENTS

To examine the environment of each object, we measured an overdensity of the surface number density of

<sup>8</sup> J135354.89+134228.5, J155846.72+223549.6, and J170441.38+604430.5.

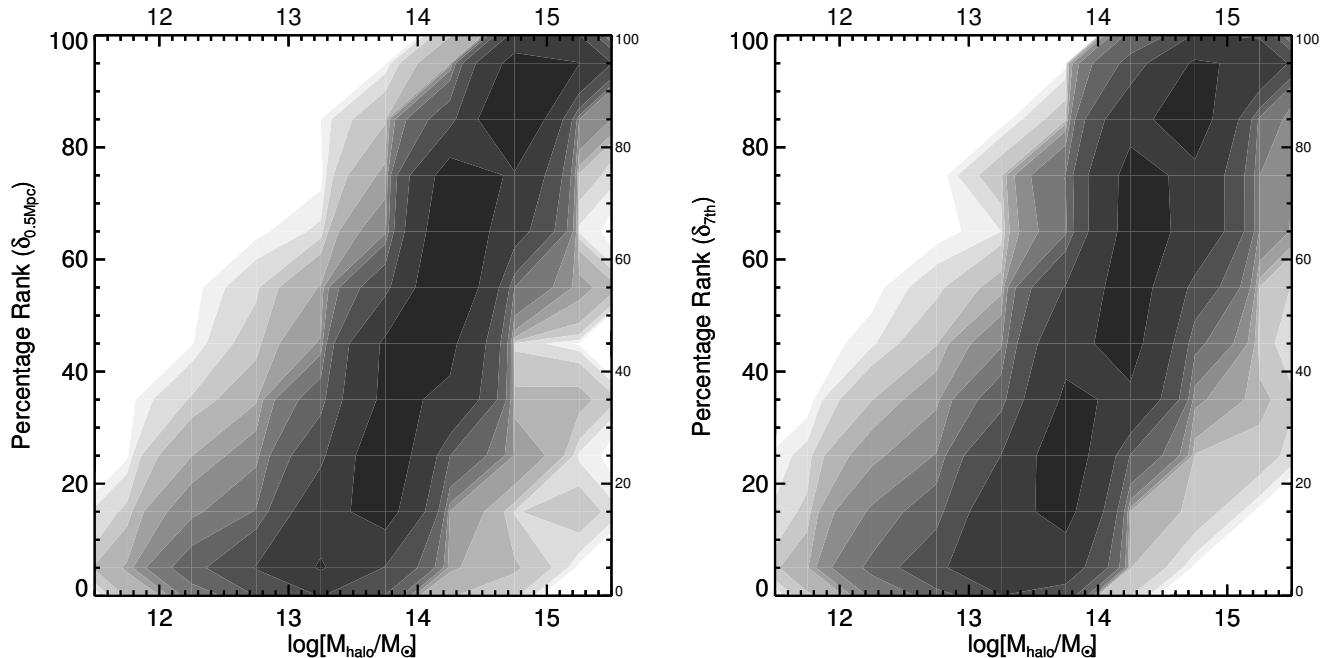


**Figure 5.** Distributions of the mock galaxies in the plane of the percentage rank of overdensities and halo mass. The left panel is for  $\delta_{0.5 \text{ Mpc}}$ , while the right panel is for  $\delta_{7\text{th}}$ . The levels of the contour represent 4, 8, 16, 32, 64, 128, 256, 512, 1024, 2048, 4096, and 8192 mock galaxies.

galaxies<sup>9</sup> in a fixed aperture (for example, an aperture with a radius of 0.5 Mpc,  $\delta_{0.5 \text{ Mpc}}$ ) or an annulus within a redshift slice. The environment measured by an aperture is known to well trace the large-scale environment external to a halo. On the other hand, the local environment internal to a halo is known to be better traced by the nearest neighbors (Muldrew et al. 2012). Therefore, to complement the aperture-based overdensity, we defined another measure of overdensity using an aperture whose radius corresponds to the projected distance to the seventh nearest galaxy ( $\delta_{7\text{th}}$ ). We chose the seventh nearest neighbor because halos with  $\log(M_{\text{halo}}/M_{\odot}) \gtrsim 13.0$  can be well identified with the environment defined by more or less the seventh nearest neighbor (Muldrew et al. 2012).

Using the MMT Hectospec data combined with the SDSS DR12 spectroscopic data, we checked the photometric redshift accuracy in order to determine the width of the redshift slice for the overdensity measurements. We calculated the rms value of the difference between the photometric redshifts and spectroscopic redshifts for the galaxies. Figure 4 shows the comparison between the photometric redshifts and spectroscopic redshifts of the galaxies. We found that the rms value of the difference between the photometric red-

shifts and the spectroscopic redshifts is  $dv \sim 8500 \text{ km s}^{-1}$  ( $\Delta z/(1+z) \sim 0.028$ ) except for  $\sim 3\%$  that are outliers. Therefore,  $dv = \pm 8500 \text{ km s}^{-1}$  is the narrowest redshift slice width in which we can plausibly argue that galaxies are lumped together in the radial direction with our photometric redshift sample, and we used a redshift slice of  $dv = \pm 8500 \text{ km s}^{-1}$  centered on the spectroscopic redshift of each quasar or galaxy throughout this study when probing the overdensity around it.

Then, the overdensity is defined by

$$\delta = \frac{\Sigma_{\text{O}} - \Sigma_{\text{B}}}{\Sigma_{\text{B}}}, \quad (1)$$

where  $\Sigma_{\text{O}}$  is the surface number density of galaxies as mentioned above.  $\Sigma_{\text{B}}$  is the background galaxy number density, which was measured as follows. Three hundred locations in the SDSS survey area were randomly chosen. For these locations, we measured the surface number density of galaxies in apertures with radii of 10 Mpc within the redshift slice of  $dv = \pm 8500 \text{ km s}^{-1}$  centered on the spectroscopic redshift of the object whose overdensity was to be measured. Finally,  $\Sigma_{\text{B}}$  was defined as the average surface number density of the 300 different locations after applying  $3\sigma$  clipping to the distribution.

The width of the redshift slice is not narrow enough to guarantee the exclusion of foreground or background interlopers. However, the background densities should appropriately account for contribution from interlopers. Furthermore, the density maps constructed from spec-

<sup>9</sup> The sample described in Section 2.3.

troscopic data follow the density maps from the photometric redshift sample (see Section 4.1).

Finally, we note that central galaxies and quasars were not included in the analysis if the aperture around them went over the SDSS survey edge in analyses. The number of such objects was 4 for quasars (0.1%) and 12 for galaxies (0.1%) when we used an aperture of a 0.5 Mpc radius.

We examined how the percentage rank of  $\delta_{0.5 \text{ Mpc}}$  or  $\delta_{7\text{th}}$  is related to halo mass with the aid of the mock galaxy lightcone catalog from the GALFORM simulation (Cole et al. 2000; Lagos et al. 2012). For this examination, we used  $\sim 185,000$  mock galaxies with  $10.5 < \log(M_{\text{bul}}/M_{\odot}) < 12.1$  in the same redshift range of  $0.24 \leq z \leq 0.40$ . We randomly extracted the mock galaxies in such a way that their bulge mass distribution was the same as the observational galaxy sample (Section 2.2), so that the bulge mass distribution mimicked that of Figure 2. The median value of the bulge masses of the mock sample is  $\log(M_{\text{bul}}/M_{\odot}) \sim 11.6$ .

We measured the overdensity values ( $\delta_{0.5 \text{ Mpc}}$  and  $\delta_{7\text{th}}$ ) of the mock galaxies in the same way as described above (hence, we also used the magnitude cut of  $M_r^e = -19.8$  for the mock galaxies in the environments). We note that the redshift values of the mock galaxies in the environments were scattered by an amount of  $\Delta z/(1+z) = 0.028$  before the measurements in order to mimic the photometric redshift uncertainty.

Figure 5 shows the distributions of the mock galaxies in the plane of the percentage rank of overdensities ( $\delta_{0.5 \text{ Mpc}}$  and  $\delta_{7\text{th}}$ ) and halo mass. We found that the percentage rank of overdensities and halo mass correlate well (the Pearson correlation coefficients are 0.88 and 0.83 for  $\delta_{0.5 \text{ Mpc}}$  and  $\delta_{7\text{th}}$ , respectively).

From this figure, we note that a percentage rank of 40% gives a good balance between completeness for the selection of clusters with  $\log(M_{\text{halo}}/M_{\odot}) > 14.0$  and the rejection of less massive halos contaminating the cluster selection. Among the galaxies in percentage ranks  $\geq 40\%$  (for both  $\delta_{0.5 \text{ Mpc}}$  and  $\delta_{7\text{th}}$ ), 88% are in  $\log(M_{\text{halo}}/M_{\odot}) \geq 14.0$ . On the other hand, among the galaxies in  $\log(M_{\text{halo}}/M_{\odot}) \geq 14.0$ , 90% are in a percentage rank  $\geq 40\%$  (for both  $\delta_{0.5 \text{ Mpc}}$  and  $\delta_{7\text{th}}$ ). We note that a percentage rank of 40% corresponds to  $\delta_{0.5 \text{ Mpc}} = 1.42$  or  $\delta_{7\text{th}} = 0.65$  for the observational galaxy sample in  $10.5 < \log(M_{\text{bul}}/M_{\odot}) < 12.1$ . Thus, we used the criteria of  $\delta_{0.5 \text{ Mpc}} = 1.42$  and  $\delta_{7\text{th}} = 0.65$  to select cluster environments with  $\log(M_{\text{halo}}/M_{\odot}) \geq 14.0$ . Note that the adopted percentage rank is rather low in comparison to what has been discussed in previous studies. For example, Muldrew et al. (2012) suggest a percentage rank of  $\gtrsim 90\%$  to select massive halos.

The difference is due to the fact that our overdensity ranks are made for the environment of galaxies with  $\log(M_{\text{bul}}/M_{\odot}) \sim 11.6$ , while their ranks are made for a complete sample of galaxies in halos with halo masses down to  $\log(M_{\text{halo}}/M_{\odot}) = 11$ . Therefore, many galaxies in less massive halos were excluded from our rank ordering, and this brought down the overdensity rank cut.

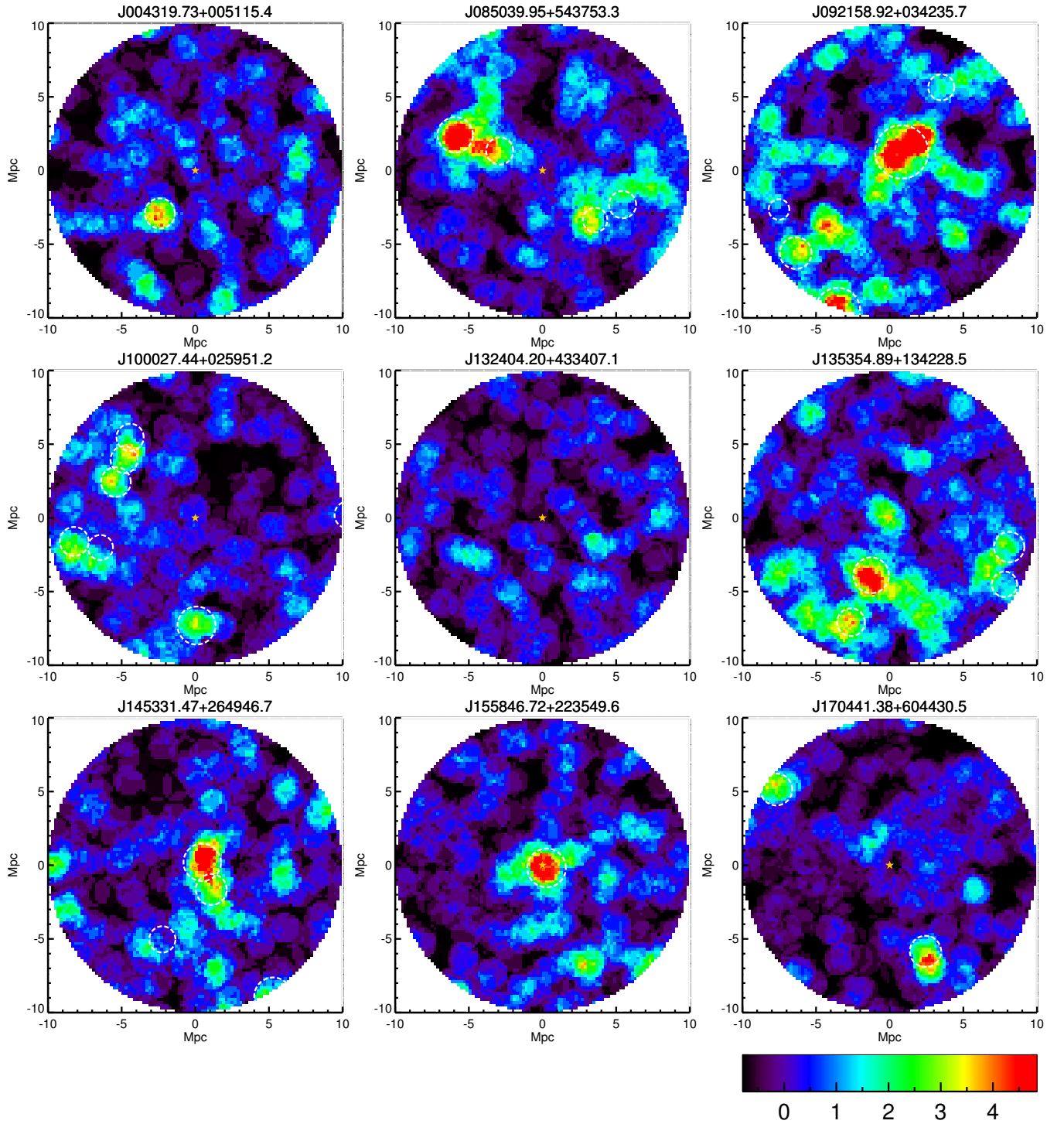
## 4. RESULTS

### 4.1. Overdensity Maps for Massive Quasars

We drew overdensity maps for the 52 massive quasars and examined large-scale structures within 10 Mpc from their centers. To construct an overdensity map, we made a grid over a rectangular area of 20 Mpc in both R.A. ( $x$  axis) and decl. ( $y$  axis), where the transverse distance scale was calculated by using the redshift of the quasar in the center of the grid. Each grid size in the  $x$  and  $y$  directions was set to be 200 kpc so that a total of  $100 \times 100$  points were generated in the grid. At each point, we measured  $\delta$  in an aperture with a radius of 1 Mpc within the redshift slice as mentioned in Section 3. Several examples of the large-scale overdensity maps we made by this procedure are shown in Figure 6. The same maps for all 52 massive quasars are shown in Figure 25 in Appendix C.

We also made overdensity maps around three massive quasars for which a Hectospec observation was performed. For this, we used only galaxies with spectroscopic redshifts, which were a combination of the galaxies observed by the Hectospec and SDSS galaxies having spectroscopic redshifts. Among these galaxies, only the galaxies that are in the redshift slice of  $dv = \pm 4000 \text{ km s}^{-1}$  centered on the spectroscopic redshift of each quasar were used. Figure 7 shows the spatial distributions of galaxies based on photometric redshifts (the upper panels) and spectroscopic redshifts (the lower panels) around the three massive quasars. These fields were chosen for Hectospec spectroscopy so that three different environments could be explored spectroscopically: a quasar embedded in an overdense environment (the left panels), a quasar not embedded in an overdense area but located close to overdense environments (the middle panels), and no significant overdense environments around a quasar (the right panels). The spatial distributions of the galaxies with spectroscopic redshifts closely follow the density maps based on photometric redshifts, especially for overdense environments, allowing the use of the overdensity based on the galaxies with photometric redshifts.




 $\delta$ 

**Figure 6.** Several examples of large-scale overdensity maps over a rectangular area of 20 Mpc in both R.A. ( $x$  axis) and decl. ( $y$  axis) around massive quasars. The colors represent the color-coded overdensities. The orange stars in the centers of the maps are the locations of quasars. The locations of known galaxy clusters are marked with circles. The radius of the circle represents  $r_{200}$  of the cluster. A figure showing the density map around the whole massive-quasar sample is given in Appendix C.

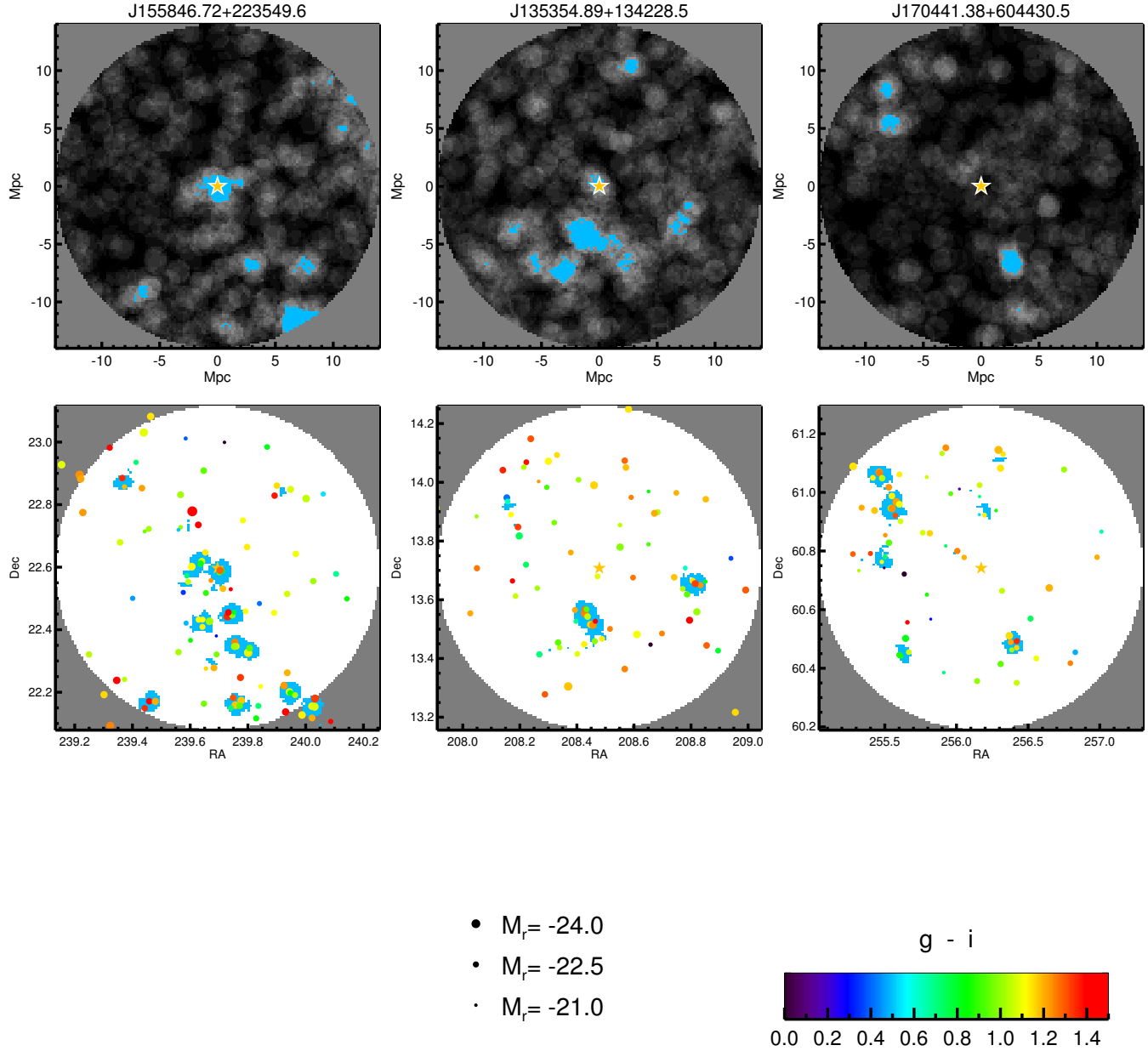


**Figure 7.** Spatial distributions of galaxies based on photometric redshifts (the upper panels) and spectroscopic redshifts (the lower panels) around three massive quasars. These fields were chosen for Hectospec spectroscopy so that three categories of different environments could be explored spectroscopically: a quasar embedded in an overdense environment (the left panels), a quasar not embedded in an overdense area but located close to overdense environments (the middle panels), and no significant overdense environments around a quasar (the right panels). The symbol size is proportional to the luminosity in the  $r$ -band. The orange stars indicate the locations of quasars. The blue regions in the overdensity maps based on photometric redshifts indicate regions of  $\delta \geq 2.5$ . On the other hand, the blue regions in the spatial distribution maps for the galaxies with spectroscopic redshifts are regions where there are three or more galaxies in a 1 Mpc aperture.

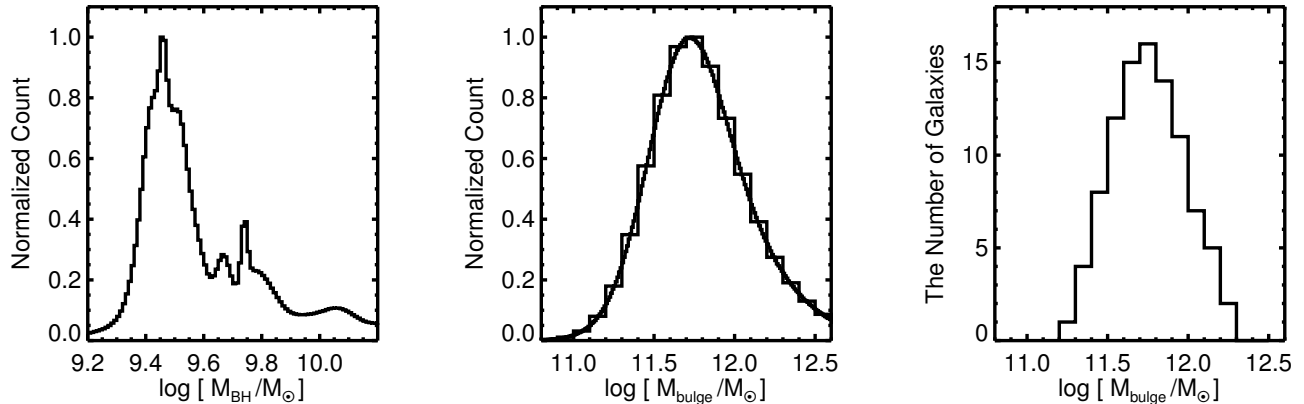


**Figure 8.** Left panel: BH mass distribution for the 52 massive quasars in which the peak is normalized to unity. Middle panel: bulge stellar mass distribution converted from the BH mass distribution in the left panel. The peak is normalized to unity. The bulge stellar mass distribution with a bin size of 0.1 dex is also plotted in the middle panel. Right panel: bulge stellar mass distribution with a total number of bulges of 95 and a bin size of 0.1 dex.

We found that massive quasars reside in various environments. Their environments can be divided into three types. Some quasars are located inside overdense environments,<sup>10</sup> while some are found in the vicinity of (or between) overdense environments.<sup>11</sup> Others have no significant overdense environments around them.<sup>12</sup>

We compared the overdensity maps we had drawn to maps in which the locations of known galaxy clusters (Wen et al. 2012) are marked. These maps with brief information (sizes and masses of the clusters) about the galaxy clusters are shown in Figure 26 in Appendix C. We also mark the locations of the clusters in Figure 6. We found that the overdensity maps based on the photometric redshifts broadly agree with the cluster maps. It is notable that there are three massive quasars that reside in massive clusters with  $\log(M_{200}/M_{\odot}) > 14.5$ : (1) two of them<sup>13</sup> reside very close to the center of the cluster of  $\log(M_{200}/M_{\odot}) = 14.5$ ; (2) the other<sup>14</sup> is located inside a very massive cluster of  $\log(M_{200}/M_{\odot}) = 14.9$ .<sup>15</sup> These cases of massive quasars in clusters are, however, not common. There are 16 such cases (30.8%) where massive quasars reside within 2 Mpc of the known-cluster centers. In 22 cases (42.3%), there are no known

clusters at the radius less than 6 Mpc from massive quasars. The remaining cases (26.9%) are in between the two cases.

#### 4.2. Comparison between Environments of Massive Quasars and Those of Mass-matched Massive Galaxies

We compared the environments of massive quasars with those of galaxies whose bulge stellar masses match the BH masses of the massive quasars through a scaling relation.<sup>16</sup> The process to extract mass-matched massive galaxies was as follows. For each quasar, we generated a normalized Gaussian distribution whose central value was the BH mass and whose  $\sigma$  was its error taken from S11. Then, these distributions were stacked to produce the BH mass distribution for the 52 quasars. The left panel of Figure 8 shows the BH mass distribution in which the peak value is normalized to unity.

We converted the BH mass distribution to the bulge stellar mass distribution using Equation (10) in Kormendy & Ho (2013). We generated  $2.6 \times 10^7$  mock BH masses that followed the BH mass distribution described above. Then, the mock BH masses were converted to the bulge stellar masses by the scaling relation. When they were converted, we considered the intrinsic scatter of the relation in the direction of the bulge stellar masses in such a way that the output values were randomly scattered by adding a random Gaussian error

<sup>10</sup> For example, J145331.47+264946.7 and J155846.72+223549.6.

<sup>11</sup> For example, J080644.42+484149.2 and J085039.95+543753.3.

<sup>12</sup> For example, J075403.60+481428.0 and J075407.95+431610.6.

<sup>13</sup> J145331.47+264946.7 and J155846.72+223549.6.

<sup>14</sup> J092158.92+034235.7.

<sup>15</sup> Here,  $M_{200}$  is the cluster mass in  $r_{200}$ , where  $r_{200}$  is the radius within which the mean density is 200 times the critical density of the universe.

<sup>16</sup> It is known that BH mass scaling relations for AGNs are almost identical to those for inactive galaxies (Woo et al. 2010; Bennert et al. 2011; Kormendy & Ho 2013; Woo et al. 2013). So we used the scaling relation derived from inactive galaxies in this study.

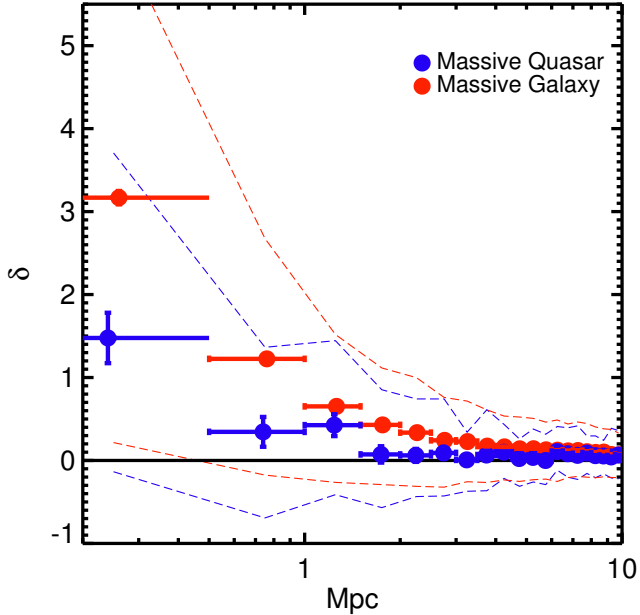


**Figure 9.** Average overdensity as a function of radial distance from massive quasars and the mass-matched massive galaxies. The blue circles indicate the 52 massive quasars, while the red circles represent the massive galaxies. The bin size is 0.5 Mpc, so that the overdensities were measured in each annulus with a width of 0.5 Mpc (indicated by the horizontal bars). The circles are slightly shifted in the  $x$  axis to avoid overlap. The dashed lines represent the 16th and 84th percentiles ( $1\sigma$ ) of the overdensities. The error of each circle is a standard deviation of the average overdensity from 1000 bootstrap resampling.

with  $\sigma = 0.22$  dex. The middle panel of Figure 8 shows the output bulge stellar mass distribution. The bulge stellar mass distribution with a bin size of 0.1 dex is also shown in the middle panel of the figure.

We then generated a bulge stellar mass distribution with a total number of bulges of 95, shown in the right panel of Figure 8.<sup>17</sup> We produced 20 sets of galaxies each containing 95 galaxies randomly selected from the galaxy sample described in Section 2.2 in the sense that they satisfy the bulge stellar mass distribution with a bin size of 0.1 dex in the right panel of Figure 8. That sample of 20 sets is the mass-matched galaxy sample (massive galaxies) of the 52 massive quasars.

We investigated the average overdensity as a function of radial distance from the massive quasars and massive galaxies, which is shown in Figure 9. In this figure,

<sup>17</sup> We set a number of 95 to avoid the repetitive selection of the galaxies more massive than  $\log(M_{\text{bul}}/M_{\odot}) = 12.1$  (only seven galaxies are such massive galaxies).

the overdensities within the distance of 0.5 Mpc from the massive galaxies are on average  $2.1 \pm 0.5$  times as high as those of the massive quasars. Furthermore, the overdensities within  $\sim 5$  Mpc from the massive galaxies are  $\sim 2$  times as high as those of the quasars. The overdensities decline as a function of distance for both massive quasars and massive galaxies and converge to the background value of 0.

Figure 10 shows the overdensity distributions (both  $\delta_{0.5 \text{ Mpc}}$  and  $\delta_{7\text{th}}$ ) for the environments of the massive quasars and massive galaxies. The distribution of the matched galaxies is skewed to higher overdensity compared to that of the massive quasars. The average  $\delta_{0.5 \text{ Mpc}}$  is  $1.5 \pm 0.3$ , while for the massive galaxies it is 3.1. On the other hand, the average  $\log(1 + \delta_{7\text{th}})$  for the massive quasars is  $0.21 \pm 0.05$ , while that of the massive galaxies is 0.46. In the case of the distribution of  $\delta_{0.5 \text{ Mpc}}$ , the probability ( $0 \leq P \leq 1$ ) of the null hypothesis, that the overdensity distribution of massive quasars and that of massive galaxies are drawn from the same distribution, is  $2.9 \times 10^{-5}$  by the Kolmogorov–Smirnov test, while it is  $1.2 \times 10^{-5}$  for the distribution of  $\delta_{7\text{th}}$ , which means the massive quasars and massive galaxies reside in essentially different environments with a significance of more than 99.99%.

However, as we shall show later in Section 5.2.1, this seemingly different distribution could be due to the lack of bulges with very high masses (the stellar mass function effect).

#### 4.3. Mass–Overdensity Relations for Quasars and Galaxies

We studied the mass–overdensity relations for the BH masses of all the quasars and the bulge stellar masses of the galaxies in the redshift range of  $0.24 \leq z \leq 0.40$  (see Section 2.1 and 2.2), which are shown in Figure 11. No sophisticated mass matching was done as in Section 4.2. The result for  $\delta_{0.5 \text{ Mpc}}$  is shown in the left panel, while the right panel shows the result for  $\delta_{7\text{th}}$ . The bulge masses for the galaxies (the upper  $x$  axis) and the BH masses for the quasars (the lower  $x$  axis) are linked by the scaling relation of Equation (10) in Kormendy & Ho (2013).

We found that galaxies with  $\log(M_{\text{bulge}}/M_{\odot}) \lesssim 11.2$  and quasars with  $\log(M_{\text{BH}}/M_{\odot}) \lesssim 9.0$  reside in similar environments, and the overdensity is nearly constant over this mass range. However, both  $\delta_{0.5 \text{ Mpc}}$  and  $\delta_{7\text{th}}$  increase rapidly at  $\log(M_{\text{bulge}}/M_{\odot}) \gtrsim 11.2$  and with quasars with  $\log(M_{\text{BH}}/M_{\odot}) \gtrsim 9.0$ . This trend is stronger for galaxies. On average, massive

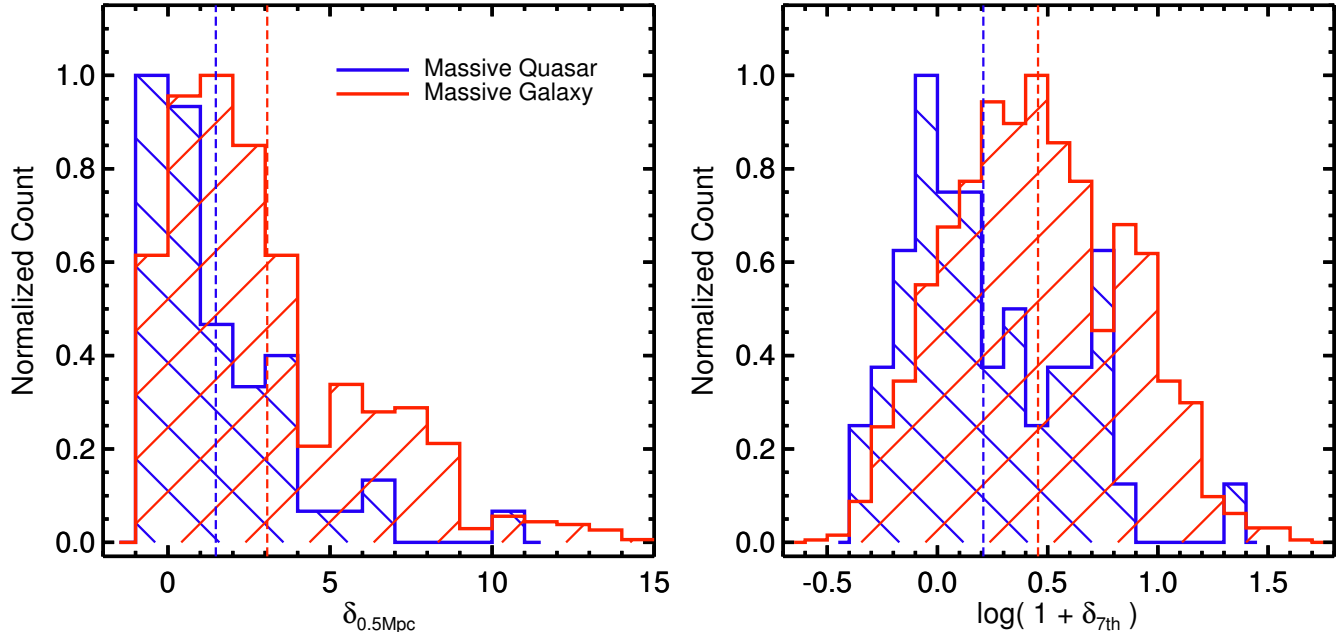


**Figure 10.** Overdensity distributions for environments of massive quasars and mass-matched massive galaxies. The peaks of the distributions are normalized to unity. The left panel shows the distributions for  $\delta_{0.5\text{Mpc}}$ , and the right panel is for  $\log(1 + \delta_{7\text{th}})$ . The blue color indicates the 52 massive quasars, while the red color represents the massive galaxies. Vertical dashed lines represent the average overdensity of each population.

quasars (massive galaxies) with  $\log(M_{\text{BH}}/M_{\odot}) \gtrsim 9.4$  ( $\log(M_{\text{bul}}/M_{\odot}) \gtrsim 11.6$ ) reside in more than  $\sim 2$  times as dense environments as their less massive counterparts with  $\log(M_{\text{BH}}/M_{\odot}) \lesssim 9.0$  ( $\log(M_{\text{bul}}/M_{\odot}) \lesssim 11.2$ ).

#### 4.4. Cluster-Finding Probability by Searching around Massive Quasars or Massive Galaxies

Here, we estimate the likelihood of finding clusters near massive quasars and massive galaxies. We investigated which massive quasars with  $\log(M_{\text{BH}}/M_{\odot}) \geq 9.4$  are in cluster environments with  $\log(M_{\text{halo}}/M_{\odot}) \gtrsim 14.0$  using the overdensity criterion of a  $\delta$  rank greater than 40%. In Section 3, we show the corresponding values of  $\delta_{0.5\text{Mpc}} \geq 1.42$  and  $\delta_{7\text{th}} \geq 0.65$ .

With  $\delta_{0.5\text{Mpc}} \geq 1.42$  or  $\delta_{7\text{th}} \geq 0.65$ , we found that 36.5% or 40.4% of massive quasars are in  $\log(M_{\text{halo}}/M_{\odot}) \gtrsim 14.0$ , respectively. If we assumed that the criteria for both  $\delta_{0.5\text{Mpc}}$  and  $\delta_{7\text{th}}$  needed to be satisfied at the same time, we would find that 25.0% of massive quasars are found in cluster environments.

We also investigated how many massive galaxies of  $\log(M_{\text{bul}}/M_{\odot}) \geq 11.6$  are in cluster environments using the same method. This mass cut corresponds to  $\log(M_{\text{BH}}/M_{\odot}) \geq 9.4$  by the scaling relation. If we chose the massive galaxies using the criteria for  $\delta_{0.5\text{Mpc}}$  and  $\delta_{7\text{th}}$  at the same time, 57.4% would be found in cluster environments. For the  $\delta_{0.5\text{Mpc}}$  and  $\delta_{7\text{th}}$  criteria, we

found that 66.9% and 69.1% of massive galaxies are in cluster environments, respectively.

From these results, we conclude that about one third of massive quasars and two thirds of galaxies with high bulge stellar masses are in dense environments with  $\log(M_{\text{halo}}/M_{\odot}) \gtrsim 14.0$  (i.e., cluster environments). Therefore, galaxies with high bulge stellar masses are better signposts for cluster environments than massive quasars.

## 5. DISCUSSION

### 5.1. Massive Quasars in Massive Clusters

As shown in the previous section, about one third of massive quasars are in cluster environments. The origin of AGN activity in such environments is intriguing, considering that galaxies in clusters tend to be poor in cold gas.

We note that similar examples, although not many, exist. The central galaxy in the cluster SPT-CL J2344-4343 (McDonald et al. 2012, 2013) and H1821+643 (Russell et al. 2010; Reynolds et al. 2014; Walker et al. 2014) are two examples. SPT-CL J2344-4343 is a massive cool-core cluster at  $z = 0.596$  with  $M_{\text{halo}} \geq 10^{15} M_{\odot}$ . The central galaxy of the cluster has a powerful AGN with a bolometric luminosity of  $\sim 10^{47} \text{ erg s}^{-1}$  and an EMBH of  $\sim 10^{10} M_{\odot}$ . Similarly, H1821+643



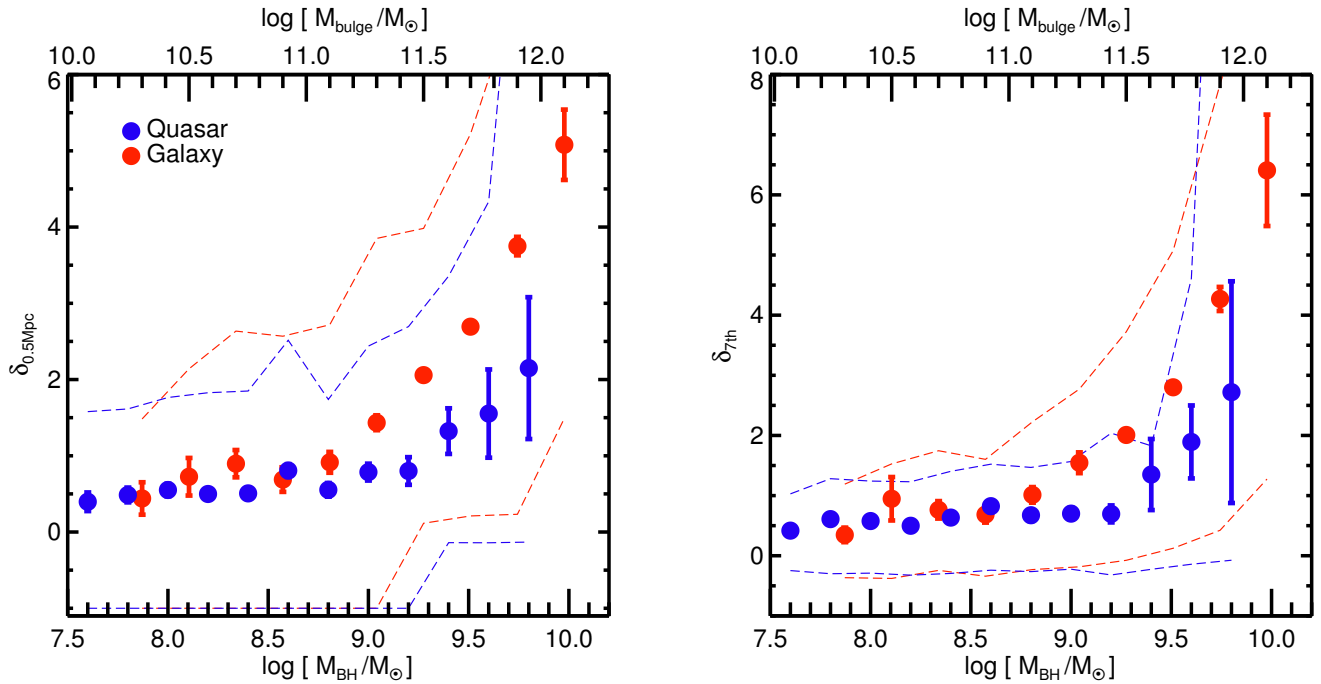


**Figure 11.** Mass-overdensity relations for BH masses of all quasars and bulge stellar masses of galaxies in the redshift range of  $0.24 \leq z \leq 0.40$ . We used the average  $\delta_{0.5\text{Mpc}}$  (the left panel) and  $\delta_{7\text{th}}$  (the right panel). The bulge masses for the galaxies (the upper  $x$  axis) and the BH masses for the quasars (the lower  $x$  axis) are linked by the scaling relation of Equation (10) in Kormendy & Ho (2013). The blue circles indicate the quasars, while the red circles are for the galaxies. The error of each circle indicates the standard deviation of the average overdensity from 1000 bootstrap resampling. The dashed lines represent the 16th and 84th percentiles ( $1\sigma$ ) of the overdensities. The bin sizes for both populations are 0.2 dex. The total number of objects in each bin is at least 10.

is a highly luminous radio-quiet quasar at  $z = 0.299$  with a bolometric luminosity of  $\sim 2 \times 10^{47} \text{ erg s}^{-1}$  and a massive BH of  $\sim 3 \times 10^9 M_{\odot}$  hosted by the central massive galaxy in a rich cool-core cluster of  $M_{500}^{18} \sim 9 \times 10^{14} M_{\odot}$ . This quasar is within the redshift range of our search but outside the SDSS coverage area. If it were in the SDSS area, we would have considered it a massive quasar in a massive cluster.

It has been suggested that the fuel of such quasars is hot plasma gas in the intracluster medium that cools down radiatively and flows into the cluster center or the central galaxy, despite the hot cluster environment (Croton et al. 2006; Fanidakis et al. 2013a,b). An alternative scenario of a merger/interaction-triggered event has been suggested too (Hutchings & Neff 1991; Fried 1998). It will be interesting to see if the host clusters of the three massive quasars we identified are cool-core clusters like these examples.

<sup>18</sup> The cluster mass in  $r_{500}$ , where  $r_{500}$  is the radius within which the mean density is 500 times the critical density of the universe at the redshift of the cluster.

## 5.2. Possible Reasons for the Environmental Discrepancy between Massive Quasars and Massive Galaxies

We discuss why the environments of massive quasars and those of massive galaxies are different. We consider several possible reasons and discuss which ones are viable.

### 5.2.1. Case 1: Bias due to Stellar Mass Function and Intrinsic Scatter in BH Mass Scaling Relation.

Here, we show that the intrinsic scatter in the BH mass scaling relation combined with the exponentially declining stellar mass function at the high-mass end can explain the environmental discrepancy between massive quasars and massive galaxies.

The main idea for this case is as follows. At the high-mass end, the numbers of high-mass galaxies and low-mass galaxies are very different simply because of the exponentially declining mass function. Then, suppose a case where we assign a BH mass to each galaxy at the high end of the bulge mass. Due to the intrinsic scatter in the scaling relation, some galaxies with higher bulge masses would have smaller BH masses, and some other

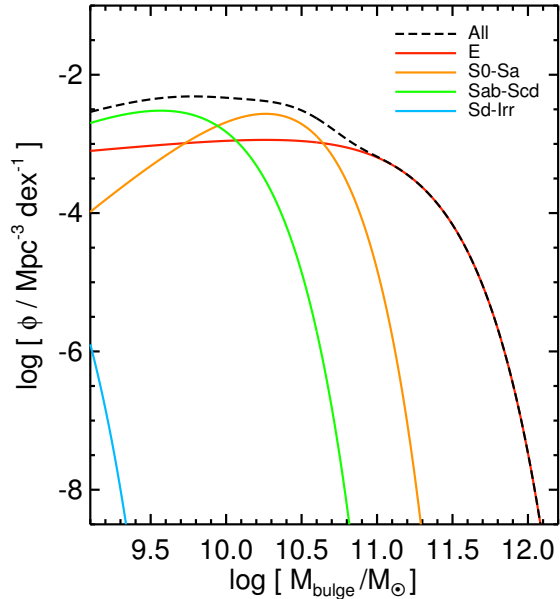


**Figure 12.** Bulge stellar mass functions for all galaxies and each Hubble type. We converted each stellar mass function to a bulge stellar mass function using the typical  $r$ -band bulge-to-total light ratio of each morphological type in Table 1 of Fukugita et al. (1998).

galaxies with lower bulge masses would have larger BH masses, with respect to the BH mass value from the BH mass scaling relation with no scatter. The net result is that, at a given BH mass, the average bulge mass of the host galaxies is less massive than the value from the BH mass scaling relation, due to the intrinsic scatter of the scaling relation applied to the unequal number of less massive and more massive bulges. Here, the major assumption is that the bulge mass is the main physical parameter, and the BH mass is a secondary parameter that derives from the BH mass scaling relation with a certain amount of intrinsic scatter. To test this scenario, we conducted a simple simulation as explained below.

First, we constructed a bulge stellar mass function from a stellar mass function using a method similar to that in Shankar et al. (2009). We used the galaxy stellar mass function for each Hubble type in Kelvin et al. (2014).<sup>19</sup> Then, we converted each stellar mass function to a bulge stellar mass function using the typical  $r$ -band bulge-to-total light ratio of each morphological type in Table 1 of Fukugita et al. (1998), assuming that the  $r$ -band bulge-to-total light ratio is equivalent to the bulge-to-total mass ratio. The adopted bulge-to-total

<sup>19</sup> They used Chabrier (2003) IMF, which is the same one used in this study.

mass ratios are 0.55, 0.30, and 0.04 for S0-Sa, Sab-Scd, and Sd-Irr, respectively. The bulge stellar mass functions for each Hubble type and their sum are shown in Figure 12.

We then generated  $\sim 4,000,000$  mock bulges that followed the bulge stellar mass function. Then, to each mock bulge, an overdensity value was randomly assigned from the overdensity values of bulges within the mass bin of 0.1 dex. After that, we converted the mock bulge stellar masses to mock BH masses using the scaling relation in Kormendy & Ho (2013), together with a random Gaussian error of  $\sigma = 0.28$  dex which corresponds to the intrinsic scatter of the  $M_{\text{BH}}-M_{\text{bulge}}$  relation from Kormendy & Ho (2013).

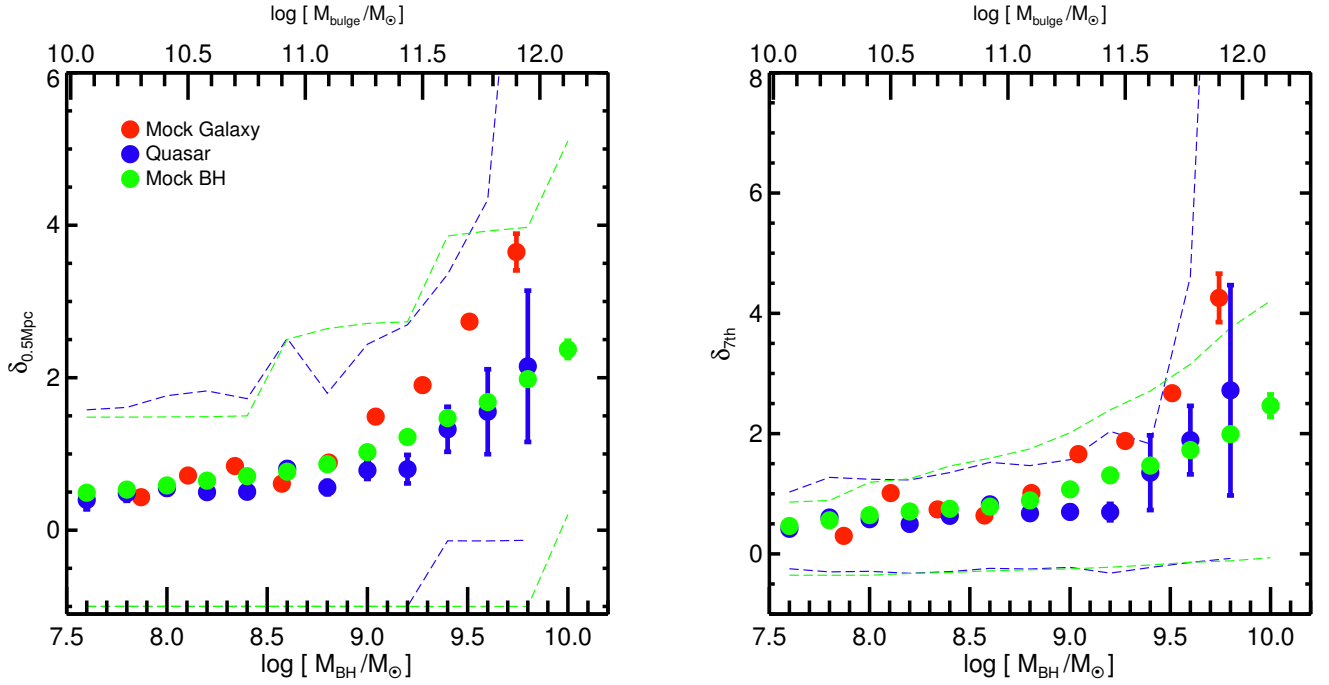
Figure 13 shows the mass-overdensity relations for quasars taken from Figure 11, the mock galaxies, and the mock BHs. In this figure, the overdensities ( $\delta_{0.5 \text{ Mpc}}$  and  $\delta_{7 \text{ th}}$ ) of the mock, inactive BHs match those of real quasars even at the massive end, although a small discrepancy is found at the mass range of  $8.9 \lesssim \log(M_{\text{BH}}/M_{\odot}) \lesssim 9.3$ . Considering the crudeness of the simulation, this small discrepancy is not surprising.

Figure 14 shows the overdensity distributions (both  $\delta_{0.5 \text{ Mpc}}$  and  $\delta_{7 \text{ th}}$ ) for the massive mock BHs and the observed quasars, both with  $\log(M_{\text{BH}}/M_{\odot}) \geq 9.4$ . In the case of  $\delta_{0.5 \text{ Mpc}}$ , the massive mock BHs and massive quasars have similar overdensity distributions with a probability of the null hypothesis of 0.17 by the Kolmogorov–Smirnov test. They have similar average overdensities too ( $1.48 \pm 0.31$  for the massive quasars and  $1.67$  for the massive mock BHs). A similar conclusion can be drawn for  $\delta_{7 \text{ th}}$ , where the probability of the null hypothesis is 0.19 by the Kolmogorov–Smirnov test, and the average  $\log(1 + \delta_{7 \text{ th}})$  is  $0.21 \pm 0.05$  for the massive quasars and  $0.26$  for the massive mock BHs.

At  $\log(M_{\text{BH}}/M_{\odot}) \geq 9.5$ , the similarity between the overdensity distributions of the two populations becomes even more significant: the two populations have the same average overdensity for both  $\delta_{0.5 \text{ Mpc}}$  and  $\delta_{7 \text{ th}}$ , and the null-hypothesis probabilities of the Kolmogorov–Smirnov test are 0.50 and 0.91 for  $\delta_{0.5 \text{ Mpc}}$  and  $\delta_{7 \text{ th}}$ , respectively.

In conclusion, this simulation shows that the introduction of the stellar mass function with the intrinsic scatter in the BH mass scaling relation gives a simple explanation for the discrepancy in the overdensities between massive quasars and massive galaxies.

If this is indeed the case, we can expect that the BH mass scaling relation is saturated at the high bulge mass end. There will be a rapid decline in the number of bulges at the high-mass end, but no such decline in



**Figure 13.** Mass-overdensity relations for observed quasars from Figure 11 (the blue circles), mock galaxies (the red circles), and mock BHs (the green circles). We used the average  $\delta_{0.5\text{Mpc}}$  (the left panel) and  $\delta_{7\text{th}}$  (the right panel). Other descriptions for this figure are the same as those for Figure 11.

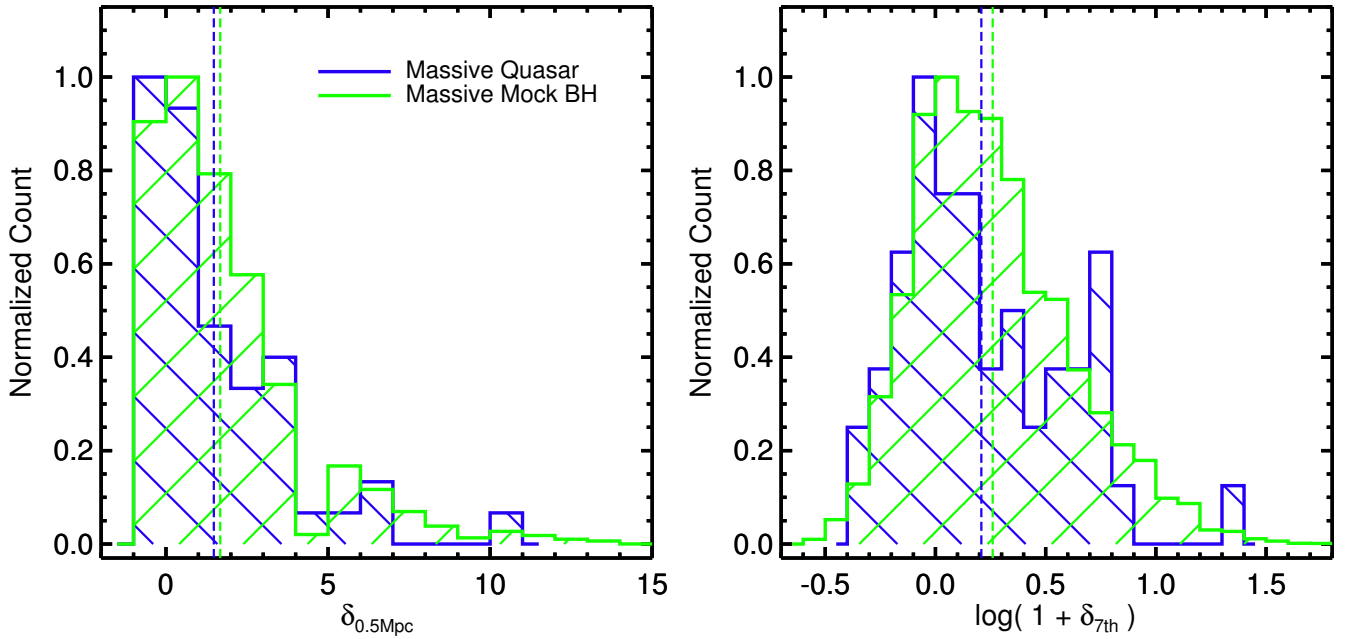


**Figure 14.** Overdensity distributions for environments of massive mock BHs and massive quasars, both with  $\log(M_{\text{BH}}/M_{\odot}) \geq 9.4$ . The peaks of the histograms are normalized to unity. The left panel shows the distributions for  $\delta_{0.5\text{Mpc}}$ . The right panel is for  $\log(1 + \delta_{7\text{th}})$ . The blue color is for massive quasars, while the green color is for the massive mock BHs. Vertical dashed lines represent the average overdensity of each population.

high-mass BHs. This appears to be the case, as can be seen in Figure 18 of Kormendy & Ho (2013). We can also predict that the bulge mass of the host galaxy of an active EMBH would be about half of what the BH mass scaling relation predicts, and this trend becomes even stronger for higher-mass EMBHs. Confirmation of this prediction can be done through an extensive study of the host galaxy mass of active EMBHs using high-resolution images (e.g., Kim et al. 2008, 2017).

### 5.2.2. Case 2: Massive Quasars and Galaxies Can Have Intrinsically Different Environments.

There have been several studies suggesting that quasars prefer group-sized, moderate environments of which the halo masses are typically in the range of  $10^{12}$ – $10^{13} M_{\odot}$  (Wold et al. 2001; Söchting et al. 2002, 2004; Coldwell & Lambas 2006; Coil et al. 2007; Myers et al. 2007; Lietzen et al. 2009; Trainor & Steidel 2012; Shen et al. 2013; Karhunen et al. 2014; Orsi et al. 2016; Song et al. 2016). Such moderate environments are also places conducive to gas-rich mergers/interactions, which are one of the main triggering mechanisms for quasars (Kauffmann & Haehnelt 2000; Canalizo & Stockton 2001; Söchting et al. 2002; Hopkins et al. 2008; Myers et al. 2008; Hong et al. 2015). A moderately dense environment is good for galaxy mergers in comparison to highly dense environments (Hashimoto & Oemler 2000), because both encounter velocities and galaxy number densities in the former are adequate for mergers (Hopkins et al. 2008; Yi et al. 2013). Moreover, galaxies in moderate environments are known to have more cold gas than those in highly dense environments (Davies & Lewis 1973; Solanes et al. 2001; Grossi et al. 2009; Catinella et al. 2013), so that SMBHs in such environments have more chance to be fueled by gas-rich mergers/interactions.

Therefore, if a gas-rich merger/interaction is the dominant quasar-triggering mechanism for the most massive quasars, this could partially explain why massive quasars live in environments less dense than those of massive galaxies. We add the word “partially” because massive quasars do live in denser environments than less massive quasars live in, and some kind of cluster-specific physical process must be in work to explain this trend.

Under this scenario, EMBHs would grow in quasar phase in moderate environments, and then later they would get incorporated into denser environments, where they would stay inactive. This scenario also expects that there should be traces of merger activity in these massive quasars in moderate environments.

### 5.2.3. Case 3: Evolution of the BH Mass Scaling Relation

Our results assume that the evolution of the BH mass scaling relation is negligible at  $z = 0$  to 0.4. However, several studies suggest that the AGN BH mass scaling relation evolves as  $M_{\text{BH}}/M_{\text{bulge}} \propto (1+z)^{\beta}$  with  $\beta$  in the range of 0.7 – 2 (Treu et al. 2004, 2007; McLure et al. 2006; Shields et al. 2006; Woo et al. 2006, 2008; Salvander et al. 2007; Jahnke et al. 2009; Bennert et al. 2010, 2011; Decarli et al. 2010; Merloni et al. 2010). This suggests that SMBHs grew in advance, and if  $\beta$  is as large as  $\sim 2$ , SMBHs in our redshift range of  $0.24 \leq z \leq 0.40$  would have been hosted by bulges that were 0.3 – 0.4 dex less massive than what the present-day scaling relation suggests. Then, it is possible to explain the environmental discrepancy between massive quasars and massive galaxies, because these  $\sim 0.3$ – $0.4$  dex less massive bulges reside in environments similar to those of massive quasars with  $\log(M_{\text{BH}}/M_{\odot}) \gtrsim 9.3$  in Figure 11.

We investigated how much the redshift evolution of the scaling relation would affect our results and whether the evolution effects can solve the environmental discrepancy between massive quasars and massive galaxies. We added an evolution effect of the scaling relation when selecting the mass-matched massive galaxies (Section 4.2). We selected  $\beta = 0.4, 0.8, 1.2, 1.6,$  and 2.0 to represent weak to strong redshift evolutions of the scaling relation. Likewise, we made various samples of mass-matched massive galaxies for the different  $\beta$  values in the same way as in Section 4.2 and compared the environments of massive quasars to those of massive galaxies.

The upper two panels of Figure 15 show the average overdensities of the mass-matched massive galaxies as a function of  $\beta$ , compared with those of the 52 massive quasars with  $\log(M_{\text{BH}}/M_{\odot}) \geq 9.4$  indicated by the blue solid lines. On the one hand, the lower two panels of Figure 15 show  $P$  from the Kolmogorov–Smirnov test as a function of  $\beta$ , where  $P$  is the probability ( $0 \leq P \leq 1$ ) of the null hypothesis that the overdensities of the massive quasars and those of the massive galaxies are drawn from the same distribution. Figure 15 shows that the average overdensities of the massive galaxies (both  $\delta_{0.5 \text{ Mpc}}$  and  $\delta_{7 \text{ th}}$ ) decrease as a function of  $\beta$ . However, they come close to the upper  $1\sigma$  of the average overdensities for the massive quasars (the upper blue dashed lines) only for cases of strong evolution ( $\beta \sim 2.0$ ). Likewise, the probability of the null hypothesis that the overdensities of the massive quasars and massive galaxies are drawn from the same distribution increases as  $\beta$  rises. When  $\beta = 2.0$ , the probabilities have values of  $P \sim 0.01$ , which indicates that the difference between the overdensity distri-

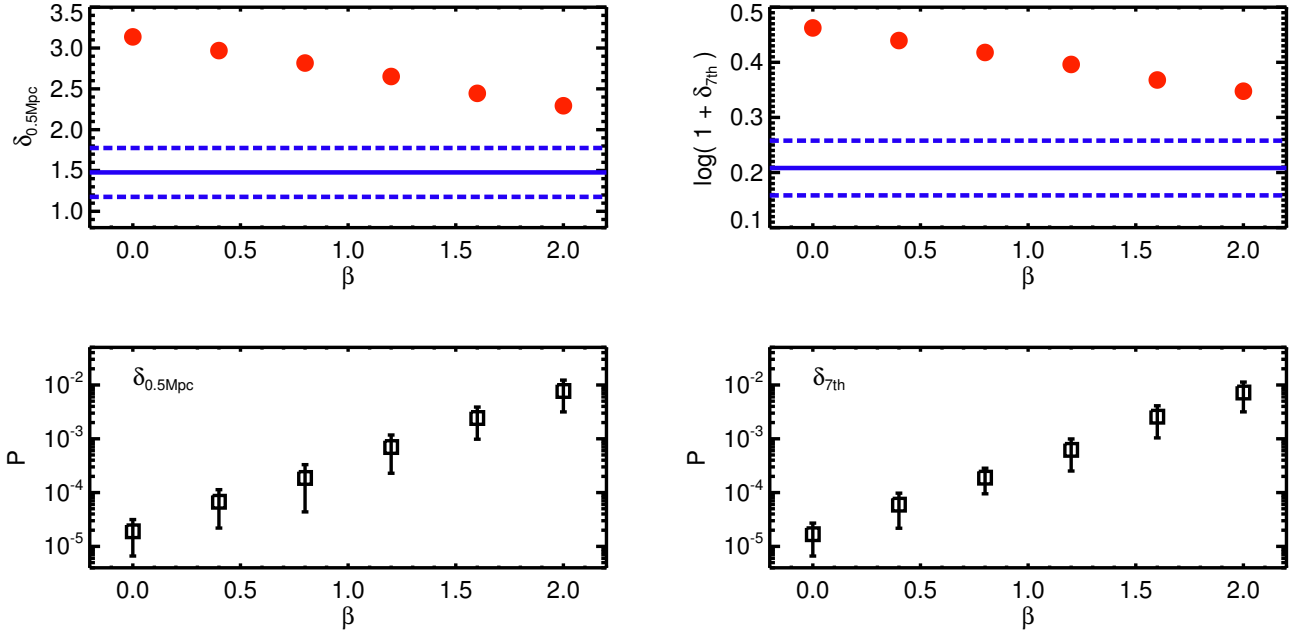


**Figure 15.** Upper two panels: average overdensities of the mass-matched massive galaxies (the red circles) as a function of  $\beta$  compared to those of the 52 massive quasars with  $\log(M_{\text{BH}}/M_{\odot}) \geq 9.4$  indicated by the blue solid lines. The blue dashed lines represent  $1\sigma$  errors of the average overdensities for the massive quasars derived by 1000 bootstrap resampling. Lower two panels:  $P$  derived by the Kolmogorov–Smirnov test as a function of  $\beta$ , where  $P$  is the probability ( $0 \leq P \leq 1$ ) of the null hypothesis that the overdensities of the massive quasars and those of the massive galaxies are drawn from the same distribution. The error of the probability is a standard deviation of probabilities from 100 trials of extracting different mass-matched massive-galaxy sample. For the overdensity measures, we used both  $\delta_{0.5\text{Mpc}}$  (the two left panels) and  $\delta_{7\text{th}}$  (the two right panels).

butions of the two populations is marginal when strong evolution is considered.

However, we consider the strong scaling relation evolution of  $\beta \sim 2$  is not plausible. Under a strongly evolving scaling relation, the host galaxy mass needs to almost double from  $z \sim 0.3$  to  $z = 0$  ( $\sim 3$  Gyr). But this is not the case according to previous observational results. For example, [van Dokkum et al. \(2010\)](#) showed that massive galaxies of  $\log(M_{\text{stellar}}/M_{\odot}) \sim 11.5$  at  $z = 0$  roughly doubled their stellar masses from  $z = 2$ , which corresponds to a time interval of  $\sim 10$  Gyr. Moreover, massive galaxies are predominantly quiescent galaxies, and their growth is dominated by dry mergers at low redshift, which only tightens the scaling relation without permitting biased growth to bulges ([Kormendy & Ho 2013](#)). Additionally, the evolution of the scaling relation may not be so effective at  $z < 1$ , because star formation and AGN activity are on the wane at that time ([Hopkins & Beacom 2006](#); [Hopkins et al. 2007](#); [Merloni & Heinz 2008](#); [Delvecchio et al. 2014](#)), preventing a rapid biased growth of either a stellar mass or a BH mass. Furthermore, even if we allow for a rapid growth of host galaxies, the host galaxies at  $z = 0$  would have properties of massive galaxies at  $0.24 < z < 0.40$  in terms of BH and stellar masses. Thus, it is very difficult to imagine such

host galaxies would have drastically different clustering properties from massive galaxies at  $0.24 \leq z \leq 0.40$ .

Therefore, we exclude the strong evolution of the scaling relation as the reason for the difference in environment between massive galaxies and massive quasars.

#### 5.2.4. Case 4: Breakdown of the BH Mass Scaling Relation at the Massive End

Scaling relations between SMBH mass and physical properties of the bulge at the massive end ( $\log(M_{\text{BH}}/M_{\odot}) \gtrsim 9.5$ ) can be uncertain due to a lack of SMBHs. If the scaling relations at the massive end were to break down, it could be the cause of the environmental discrepancy between massive quasars and massive galaxies.

It has been found that the  $M_{\text{BH}}-\sigma$  relation is indeterminate at  $\sigma \gtrsim 270 \text{ km s}^{-1}$  ([Lauer et al. 2007](#); [Kormendy & Ho 2013](#); [McConnell & Ma 2013](#)), due to the lack of galaxies with  $\sigma \gtrsim 270 \text{ km s}^{-1}$ , while BH masses continue to increase over this scaling relation limit.

However, the  $M_{\text{BH}}-M_{\text{bulge}}$  relation we use here does not show notable breakdown and is valid even at the massive end of  $\log(M_{\text{bulge}}/M_{\odot}) \sim 11.8$  and  $\log(M_{\text{BH}}/M_{\odot}) \sim 9.6$  (see Figure 17 in [Kormendy & Ho \(2013\)](#)). This is supported by [Lauer et al. \(2007\)](#),



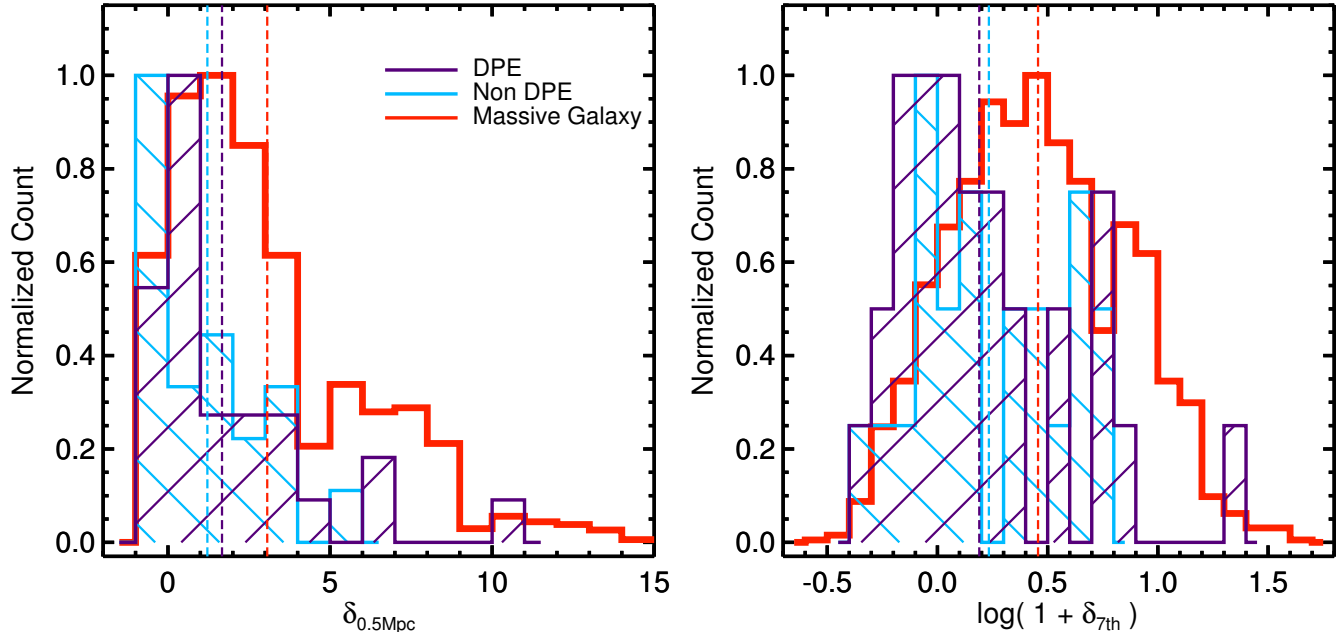


**Figure 16.** Overdensity distributions for environments of DPEs, non-DPEs, and the mass-matched massive galaxies in Section 4. The peaks of the histograms are normalized to unity. The left panel shows the distributions for  $\delta_{0.5\text{Mpc}}$ . The right panel is for  $\log(1 + \delta_{7\text{th}})$ . Vertical dashed lines represent the average overdensity of each population.

who argue that the  $M_{\text{BH}}-L_{\text{bulge}}$  relation is a more reliable description for massive, high-luminosity galaxies than  $M_{\text{BH}}-\sigma$  relation, because the BH mass to stellar mass ratio for massive galaxies hardly changes in the process of a dissipationless merger, which frequently happens in massive galaxies. Therefore, we suggest that the breakdown of the  $M_{\text{BH}}-M_{\text{bulge}}$  relation at the massive end is not the main reason for the environmental discrepancy between the two populations. The scaling relation, however, can show a lack of massive host galaxies which mimics a steepening of the relation at massive end as explained in Section 5.2.1.

#### 5.2.5. Case 5: Uncertainty of BH and Stellar Mass Measurements

If the BH masses are poorly measured quantities with larger errors than expected, then the large errors will act like intrinsic scatter and dilute the clustering signal. In other words, BH mass can be as good a proxy as stellar mass for the local overdensity, but the observed clustering signal of a given BH mass, when its measurement error is unexpectedly large, can reflect that of a lower-mass BH because there are more lower-mass BHs that scatter into the high-mass part than the higher-mass BHs that scatter into the low-mass part. A large uncertainty in stellar mass measurements can lead to a similar conclusion. This kind of bias is not built into our analysis in Section 4, but the effect should

be nearly identical to what we learned in the previous subsection about how the intrinsic scatter of the BH mass scaling relation and the shape of the stellar mass function affect the clustering signal. So, we leave this possibility of the BH mass having a larger measurement uncertainty as a plausible cause for the discrepancy between the environments of massive quasars and galaxies.

#### 5.2.6. Case 6: Environment of Quasars with and without Double-peaked Broad Emission Lines

Some AGNs, especially those with large velocity widths, are known to have abnormally asymmetric or double-peaked broad emission lines. Several studies explain double-peaked broad emission lines by relativistic accretion disks around SMBHs (Chen et al. 1989; Eracleous & Halpern 1994; Strateva et al. 2003), while others suggest binary SMBHs as the origin of the profile shape (Gaskell 2010; Shen & Loeb 2010). The BH masses of AGNs having double-peaked broad emission lines are also suggested to have been overestimated by a factor of a few (Zhang et al. 2007; Jun et al. 2017). Given that many EMBHs have large FWHM velocity widths, many of them can have double-peaked broad emission lines and overestimated BH masses. To see if this is the reason for the overdensity discrepancy, we selected massive quasars with double-peaked broad emission lines (hereafter, DPEs) and examined their environments

versus those of massive quasars without double-peaked broad emission lines (hereafter, non-DPEs).

We classified a broad  $H\beta$  line as double-peaked when there were broad-line components that were shifted more than  $2500 \text{ km s}^{-1}$  from the center of the narrow-line component and the sum of the line luminosities of these shifted components was more than 10%<sup>20</sup> of the total broad-line luminosity (see Appendix A for the line-fitting procedure). By this criterion, 30 massive quasars (58% of the massive quasars) were classified as DPEs (see Table 1).

In Figure 16, we show the overdensity distributions for the DPEs, the non-DPEs, and the mass-matched massive galaxies in Section 4. The DPEs and non-DPEs have similar overdensity distributions with a null-hypothesis probability of the Kolmogorov–Smirnov test of 0.58 and 0.79 for  $\delta_{0.5 \text{ Mpc}}$  and  $\delta_{7\text{th}}$ , respectively. The average overdensities for the DPEs and non-DPEs are also consistent with each other ( $\delta_{0.5 \text{ Mpc}} = 1.22 \pm 0.35$  for the non-DPEs and  $\delta_{0.5 \text{ Mpc}} = 1.67 \pm 0.45$  for the DPEs, and  $\log(1 + \delta_{7\text{th}}) = 0.23 \pm 0.07$  for the non-DPEs and  $\log(1 + \delta_{7\text{th}}) = 0.19 \pm 0.07$  for the DPEs).

We conclude that it does not help to reduce the overdensity discrepancy problem by treating DPEs and non-DPEs separately, which suggests that the overestimation of BH mass for DPEs is not very significant or that the BH masses of DPEs and non-DPEs are similarly biased/unbiased.

### 5.2.7. Summary of Reasons for the Environmental Discrepancy

In the subsections above, we investigate six possible reasons for the environmental discrepancy between massive quasars and massive galaxies. The different environments between them can be explained simply with the exponentially declining stellar mass function at the high bulge mass end combined with the intrinsic scatter of the BH mass scaling relation or the uncertainty of BH mass measurements. Alternatively, if quasars are mainly triggered by gas-rich processes that prefer group-scale environments, this may partially explain the environmental discrepancy. The redshift evolution of the BH scaling relation, the breakdown of the scaling relation, and DPEs versus non-DPEs are unlikely to be the reason for the environmental discrepancy.

<sup>20</sup> We changed this criterion to 50% and tried the analysis in the same way. By the modified criterion, 20 quasars were classified as the DPEs, while 32 quasars were non-DPEs. However, there was no meaningful change in our results. Thus, we used the conservative criterion of 10% in this study.

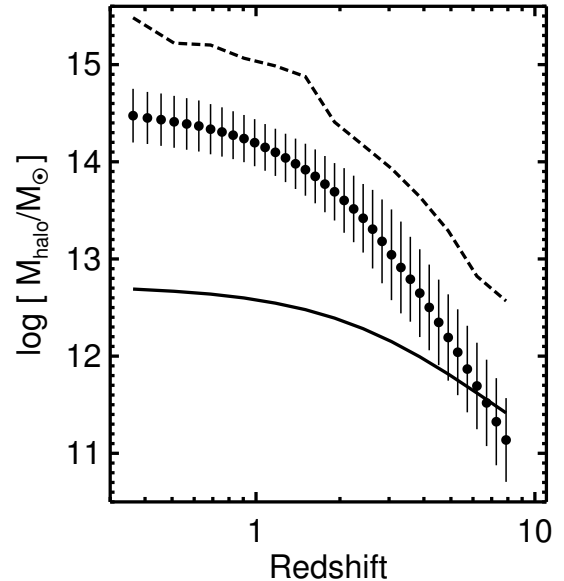


**Figure 17.** Average halo mass as a function of redshift for progenitors of the 492 EMBHs of  $\log(M_{\text{BH}}/M_{\odot}) > 9.4$  at  $z = 0.36$ . The error bars are standard deviations of the halo masses. The solid line represents the top 1% halo mass among the halos of  $\log(M_{\text{halo}}/M_{\odot}) \geq 10.5$ , while the dashed line indicates the most massive halo in each epoch.

As we could not find a definitive reason, further investigations are needed to identify the most plausible cause for the environmental discrepancy between massive quasars and massive galaxies. For example, the morphology of the host galaxies of active EMBHs can shed light on this problem. If the difference in environment is due to the gas-rich triggering mechanism of quasars preferred in group-scale environments, active EMBHs would be hosted mostly by gas-rich merging galaxies. On the other hand, if the difference in environment is simply due to the exponentially declining stellar mass function at the high bulge mass end combined with the intrinsic scatter of the BH mass scaling relation or the uncertainty of BH mass measurements, then active EMBHs are more likely to be in hot-halo mode, and thus the fraction of gas-rich merger hosts would be low. Future analysis of large simulation datasets implementing an AGN component will help to better define the expected properties of the environment of active EMBHs.

### 5.3. Comparison with Lambda Cold Dark Matter Galaxy Formation Simulation

In Section 1, we mention that active EMBHs at  $z \lesssim 1$  are likely to be in a dense environment, according to a

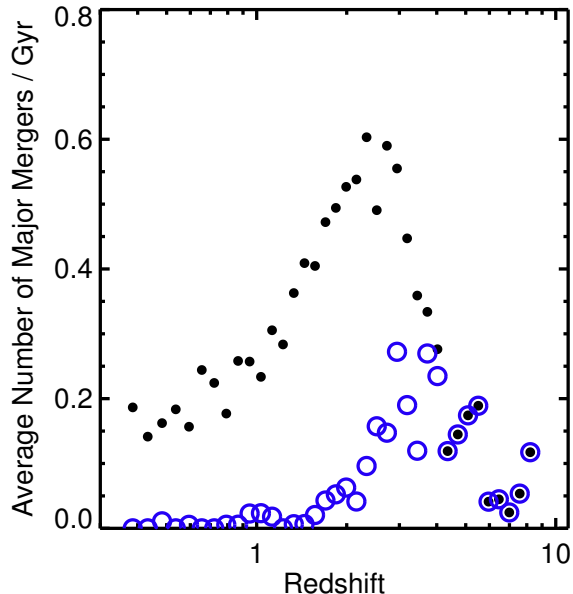


**Figure 18.** Average number of major mergers (the black points) and gas-rich major mergers (the blue circles) the EMBHs of  $\log(M_{\text{BH}}/M_{\odot}) > 9.4$  at  $z = 0.36$  have experienced in a Gyr.

simulation result. According to our observation, this is not exactly the case, because we found quite a few massive quasars in moderate to low density environments. One way to reconcile the data with the simulation result is to consider that some massive quasars are hosted by less massive galaxies and in less massive halos due to the nature of the BH mass scaling relation as discussed in Section 5.2.1. Another possibility is that the mass of many active EMBHs is not as massive as we think. In such a case, only a small portion of active EMBHs are truly EMBHs, and the rest are less massive BHs in moderate environments.

Further insight can be gained by examining other simulations. We examined how EMBHs grew using the lambda cold dark matter galaxy formation simulation of Guo et al. (2011) based on the Millennium 1 Simulation (Springel et al. 2005). In this simulation, SMBHs grow via BH mergers, cold-gas accretion during gas-rich mergers, or hot-gas accretion in halos. The simulation does not identify which SMBHs are undergoing AGN activity. However, at the least, we can assume that gas-rich mergers produce AGN activity.

In the simulation, we identified 492 EMBHs of  $\log(M_{\text{BH}}/M_{\odot}) > 9.4$  in the snapshot volume at  $z = 0.36$ . Then, we traced main progenitors that were the most massive progenitors in the merger tree of each EMBH and extracted the halo masses in which the pro-

genitors resided. Figure 17 shows the average halo mass as a function of redshift for the main progenitors of the 492 EMBHs. This figure shows that the EMBHs at  $z = 0.36$  are in massive halos of  $\log(M_{\text{halo}}/M_{\odot}) \gtrsim 14$ . In the simulation, we identified that 2 out of the 492 EMBHs experienced a recent gas-rich major merger in  $\sim 1$  Gyr. These EMBHs in the gas-rich major merger phase can be identified as massive quasars. The halo mass of one such quasar is  $M_{\text{halo}} \sim 10^{13.6} M_{\odot}$ , and another is  $M_{\text{halo}} \sim 10^{15.2} M_{\odot}$ .

The trend of the progenitors of EMBHs at  $z = 0.36$  being found in massive halos continues to  $z \sim 2$ . Unfortunately, the volume of the simulation data is not large enough to contain EMBHs at  $z \gtrsim 1$ . So, we could not directly infer the environment of EMBHs at high redshifts. We noticed that these EMBH progenitors are also the most massive BHs at  $z \lesssim 2$  in the simulation. Therefore, we expect that many active/inactive EMBHs would also be in massive halos at  $z \lesssim 2$  in the simulation. However, at  $z \gtrsim 4$ , the halos of the EMBH progenitors are not as massive as those at  $z \lesssim 2$ . This suggests that massive quasars are not in massive halos at  $z \gtrsim 4$ ; the analysis of Fanidakis et al. (2013b) suggests the same.

Furthermore, we examined the way in which these EMBHs grew. Figure 18 shows the average number of major mergers and gas-rich mergers EMBHs have experienced in a gigayear. We analyzed the merger histories of EMBHs of  $\log(M_{\text{BH}}/M_{\odot}) > 9.4$  at  $z = 0.36$  and counted the number of major mergers that each EMBH had experienced. We classify a merger as a major merger when the mass ratio of the progenitors is higher than 0.3. A major merger is defined as a gas-rich major merger when the total cold-gas mass of the progenitors is larger than half of the total stellar mass of the progenitors.<sup>21</sup> Otherwise, it is defined as a dry merger. Figure 18 shows that, at  $z \lesssim 2$ , the growth of EMBHs is mainly achieved through a dry merger that is not expected to accompany strong AGN activity. The gas-rich major merger becomes important at  $z \gtrsim 4$ , which coincides with the epoch when the EMBH growth occurs in less massive halos. Again, these results roughly agree with the prediction of Fanidakis et al. (2013b), and we expect that active EMBHs are not in massive halos at  $z \gtrsim 4$ . Observational results appear to agree with such a conclusion (e.g., Kim et al. 2009; Bañados et al. 2013; Husband et al. 2013; Simpson et al. 2014; Uchiyama et al. 2018).

<sup>21</sup> If a looser criterion (a ratio of the total cold-gas mass to the total stellar mass  $\geq 0.25$ ) is adopted, the epoch in which gas-rich major mergers are dominant is changed to  $z \gtrsim 3$ . However, it does not essentially change our main results in this section.

Overall, the simulation results suggest that active EMBHs are mostly in massive halos at  $z \lesssim 2$  but not so at  $z \gtrsim 4$ . Our current observational result does not agree with this prediction at  $z = 0.36$ . More extensive investigation of simulation data sets is needed to reach firm conclusion about this issue.

## 6. SUMMARY

We have investigated the environments of 9461 galaxies and 2943 quasars at  $0.24 \leq z \leq 0.40$ . In addition, we have compared the environments of massive quasars with those of galaxies with comparable BH masses.

Our results are summarized below.

1. Massive quasars (massive galaxies) with  $\log(M_{\text{BH}}/M_{\odot}) \gtrsim 9.4$  ( $\log(M_{\text{bul}}/M_{\odot}) \gtrsim 11.6$ ) reside in environments more than  $\sim 2$  times as dense as their less massive counterparts with  $\log(M_{\text{BH}}/M_{\odot}) \lesssim 9.0$  ( $\log(M_{\text{bul}}/M_{\odot}) \lesssim 11.2$ ).
2. Massive galaxies are in denser environments than massive quasars. About two thirds of massive galaxies were found to reside in galaxy clusters. However, only one third of massive quasars were found to be associated with galaxy clusters. Massive quasars ( $\log(M_{\text{BH}}/M_{\odot}) \geq 9.4$ ) reside in about  $\sim 2$  times underdense environments compared with massive galaxies with comparable BH masses.
3. The seemingly different environments between massive quasars and massive galaxies can be explained naturally with the exponentially declining stellar mass function at the high bulge mass end in combination with the intrinsic scatter of the BH mass scaling relation or the uncertainty of BH mass measurements.
4. Alternatively, massive quasars may be more preferentially found in less massive environments because their existence calls for gas-rich mergers that occur more often in group-scale environments. Other alternatives, such as the redshift evolution of the BH scaling relation, the breakdown of the scaling relation, and DPEs versus non-DPEs, are unlikely to be responsible for the environmental discrepancy between massive quasars and massive galaxies.
5. Simulation data suggest EMBHs at  $z = 0.36$  reside in massive halos of  $\log(M_{\text{halo}}/M_{\odot}) \gtrsim 14$  in their growth histories out to  $z \sim 2$ . Active EMBHs are also expected to reside mainly in such environments. This simulation prediction appears to

be inconsistent with our result that many massive quasars are located in moderate to low density environments.

Massive quasars do live in environments denser than where less massive quasars reside. This implies that some EMBHs become active in dense environments in hot-halo mode. However, while the majority of inactive EMBHs are in dense environments, we show the puzzling fact that about two thirds of active EMBHs are in moderate to low density environments, in contrast to some simulation results. The reason for this result needs to be understood through future investigations. Also, the prevalence of active EMBHs in moderate to low density environments indicates the limited usefulness of active EMBHs for identifying overdense regions at higher redshifts.

This research was supported by Basic Science Research Program through the National Research Foundation of Korea (NRF), funded by the Ministry of Education (NRF-2017R1A6A3A04005158). M.H. acknowledges support from Global PhD Fellowship Program through the NRF, funded by the Ministry of Education (NRF-2013H1A2A1033110). This work used data taken under the K-GMT Science Program (PID: mmt-2015A\_00006) of the Korea Astronomy and Space Science Institute. The observations reported here were obtained at the MMT Observatory, a joint facility of the University of Arizona and the Smithsonian Institution. Funding for SDSS-III was provided by the Alfred P. Sloan Foundation, the Participating Institutions, the National Science Foundation, and the US Department of Energy Office of Science. The SDSS-III website is located at <http://www.sdss3.org/>. SDSS-III is managed by the Astrophysical Research Consortium for the Participating Institutions of the SDSS-III Collaboration, including the University of Arizona, the Brazilian Participation Group, Brookhaven National Laboratory, Carnegie Mellon University, University of Florida, the French Participation Group, the German Participation Group, Harvard University, the Instituto de Astrofísica de Canarias, the Michigan State/Notre Dame/JINA Participation Group, Johns Hopkins University, Lawrence Berkeley National Laboratory, Max Planck Institute for Astrophysics, Max Planck Institute for Extraterrestrial Physics, New Mexico State University, New York University, Ohio State University, Pennsylvania State University, University of Portsmouth, Princeton University, the Spanish Participation Group, University of Tokyo, University of Utah, Vanderbilt

University, University of Virginia, University of Washington, and Yale University. The Millennium Simulation databases used in this paper and the web application providing online access to them were constructed as part of the activities of the German Astrophysical Virtual Observatory.



## APPENDIX

## A. BH MASS MEASUREMENTS FOR 52 MASSIVE QUASARS AND COMPARISON WITH RESULTS FROM SHEN ET AL. (2011)

We measured BH masses using broad H $\beta$  lines for the 52 massive quasars to examine the reliability of the BH mass measurements by S11 at the massive end. We describe our BH mass measurements in this section.

First, Galactic extinctions in the line of sight were corrected for the quasar spectra using the dust map of Schlegel et al. (1998) and the Galactic extinction curve from Fitzpatrick (1999) assuming  $R_V = 3.1$ . We fit the continuum and the blended broad iron lines using the combination of a power-law continuum, and an iron template. We set the power law in the functional form of  $f_\lambda = \alpha\lambda^\beta$ , where  $\alpha$  is the normalization constant and  $\beta$  is the continuum slope. For the iron template, we assumed three parameters: the normalization, the velocity width, and the offset of the iron template, for which we adopted the template of Boroson & Green (1992). The continuum fit was conducted in two windows: a shorter-wavelength window of  $4435 \leq \lambda \leq 4625 \text{ \AA}$  and a longer-wavelength window of  $5100 \leq \lambda \leq 5535 \text{ \AA}$ .

We fit the narrow [O III]  $\lambda\lambda 4959, 5007$  lines with two Gaussian functions for each line: one for a core component and the other for a blue-wing component, given that many [O III]  $\lambda\lambda 4959, 5007$  lines have extended wings at a shorter wavelength of the lines (Greene & Ho 2005; Komossa et al. 2008). The narrow H $\beta$  lines were modeled with a single Gaussian function. We set an upper limit of  $1200 \text{ km s}^{-1}$  for the FWHM of all the narrow lines. Fixed were the relative velocity offsets between the narrow H $\beta$  line and each of the core [O III]  $\lambda\lambda 4959, 5007$  lines. Additionally, the same FWHM for the core [O III]  $\lambda\lambda 4959, 5007$  lines was assumed. At the same time, the blue-wing components for [O III]  $\lambda\lambda 4959, 5007$  were set to have the same FWHM values. The velocity offsets of the blue-wing components from core [O III]  $\lambda\lambda 4959, 5007$  lines were tied together. For the broad H $\beta$  lines, we fit multi-Gaussian functions with up to three components, and a lower limit of  $1200 \text{ km s}^{-1}$  was set for the FWHM of each component. The line fitting was conducted in the wavelength window of  $4700 \leq \lambda \leq 5100 \text{ \AA}$ .

Using the FWHMs of the multi-Gaussian functions and the continuum luminosity at  $5100 \text{ \AA}$ , we derived virial BH masses using the calibration expression from Vestergaard & Peterson (2006):

$$\log\left(\frac{M_{\text{BH}}}{M_\odot}\right) = 0.50 \log\left(\frac{\lambda L_\lambda}{10^{44} \text{ erg s}^{-1}}\right) + 2 \log\left(\frac{\text{FWHM}_{\text{H}\beta}}{\text{km s}^{-1}}\right) + 0.91, \quad (\text{A1})$$

where  $\lambda = 5100 \text{ \AA}$ , so  $\lambda L_\lambda = L_{5100}$ . The uncertainties of the measured masses of SMBHs were estimated by 100 mock spectra, which were generated by adding Gaussian noises to an original spectrum using the flux density errors.<sup>22</sup> We fit the 100 mock spectra by the same fitting method as described above. Then, we adopted an estimated standard deviation of the virial BH masses after  $3\sigma$  clipping as the uncertainty of the BH mass. Likewise, we estimated the uncertainties of the  $L_{5100}$  and FWHM of the broad H $\beta$  line. The fitting results for the 52 massive quasars are shown in Figure 19.

The left panel of Figure 20 compares the BH mass estimates from S11 and our measurements. We conducted a linear fit with errors in both variables. When the slope is fixed to unity, the zero-point offset from the one-to-one relation is  $-0.08 \pm 0.02$  dex, which means our measurements are slightly smaller than the S11 values. When the slope is not fixed, the slope of the linear relation is  $0.81 \pm 0.10$ , and the intrinsic scatter of the linear relation is 0.13 dex. The middle panel of Figure 20 shows the comparison of  $L_{5100}$  estimates between S11's and our measurements. We conducted a linear fit with errors in both variables. When the slope is fixed to unity, the zero-point offset from the one-to-one relation is  $-0.004 \pm 0.004$  dex. When the slope is not fixed, the slope of the linear relation is  $1.01 \pm 0.01$ , and the intrinsic scatter of the linear relation is 0.03 dex. The  $L_{5100}$  values from S11 and our measurements agree well. For logarithmic values of the FWHMs (the right panel of Figure 20), the zero-point offset from the one-to-one relation when the slope is fixed to unity is  $-0.04 \pm 0.01$  dex. When the slope is not fixed, the slope of the linear relation is  $0.77 \pm 0.07$ , and the intrinsic scatter of the linear relation is 0.06 dex. Therefore, the slight difference in BH mass estimates from S11 and our analysis mostly originates from the difference in FWHM estimates.

We scrutinized nine quasars whose BH masses from S11 are exceptionally larger ( $> 0.3$  dex) than our estimates. Six quasars<sup>23</sup> among them were found to have very large H $\beta$  FWHM values in S11 (FWHM  $> 25,000 \text{ km s}^{-1}$ ). S11 fit

<sup>22</sup> This is the same method as in S11. We note that the uncertainties measured by this method are conservative errors, as they were derived by adding noise to the original spectrum.

<sup>23</sup> J031332.88-063157.9, J101226.85+261327.2, J102738.53+605016.4, J125105.07+380744.3, J150019.08+000249.0, and J154426.06+000923.5.

these lines with an extremely broad single Gaussian function (or double Gaussian functions not much different from a single Gaussian function), despite the fact that these lines show complex features, such as double peaks. These fits resulted in overestimates of  $H\beta$  FWHM values. Examination of the  $H\alpha$  line shape also shows that our fits with more than two Gaussian components represent the line shapes much better. In the case of the other three quasars,<sup>24</sup> a different treatment in the [O III] line shape and/or the continuum fit gave S11 FWHM values much larger than ours, resulting in the difference in BH masses. To see how the re-analysis of the SDSS spectra would affect the main results of the paper, we repeated all of our analyses using the BH mass values we estimated. However, there was no meaningful change in our results, suggesting that re-analysis of the BH masses for the full sample is not necessary.

## B. RESULTS BASED ON BROAD $H\alpha$ LINE

Here, we use broad  $H\alpha$  lines for the BH mass estimation and present the results based on these BH masses. As shown in Appendix A, the FWHM measurement of the broad  $H\beta$  line is a key factor for BH mass measurements. Since broad  $H\alpha$  lines have much higher S/N values than the broad  $H\beta$  lines, using them gives us a chance to check the reliability of BH mass measurements based on the broad  $H\beta$  lines as well as complementary results. Unfortunately, broad  $H\alpha$  lines or the required wavelength ranges for the fit are beyond or at the end of the SDSS spectral coverage ( $\sim 9200\text{\AA}$ ) for quasars in the redshift range of  $0.24 \leq z \leq 0.40$ . Therefore, we restricted the redshift range of our sample to  $0.24 \leq z \leq 0.31$  in order to select a reliable broad  $H\alpha$  line fit. Using the FWHM values of the broad  $H\alpha$  lines and the continuum luminosity at  $5100\text{\AA}$  from S11, we derived BH masses using the expression from Jun et al. (2017):

$$\log\left(\frac{M_{\text{BH}}}{M_{\odot}}\right) = 0.533 \log\left(\frac{\lambda L_{\lambda}}{10^{44} \text{ erg s}^{-1}}\right) + 2.12 \log\left(\frac{\text{FWHM}_{H\alpha}}{\text{km s}^{-1}}\right) + 0.69, \quad (\text{B2})$$

where  $\lambda = 5100\text{\AA}$ , so  $\lambda L_{\lambda} = L_{5100}$ .

Figure 21 shows a comparison between BH masses measured by  $\text{FWHM}_{H\beta}$ <sup>25</sup> and those measured by  $\text{FWHM}_{H\alpha}$ . The total number of the data points is 1020. The linear fit line has a slope of  $0.96 \pm 0.01$ , and the intrinsic scatter of the linear relation is 0.14 dex. When the slope is fixed to unity, the zero-point offset from the one-to-one relation is  $0.03 \pm 0.01$  dex. We found that the two estimates are consistent with each other.

There are 18 quasars with  $\log(M_{\text{BH}}(H\alpha))/M_{\odot} \geq 9.4$  in our sample. We analyzed these in the same way as in Section 4. The results are shown in Figures 22–24, where we show the overdensity–radius relation, the overdensity distributions, and the mass–overdensity relations, respectively. In these figures, we also plot the results for massive quasars with  $H\beta$ -derived BH masses. All these  $H\alpha$ -based results are nearly identical to the  $H\beta$ -based results. In conclusion, even if we used BH masses measured by broad  $H\alpha$  lines, the main results would be almost identical to those of broad  $H\beta$  lines.

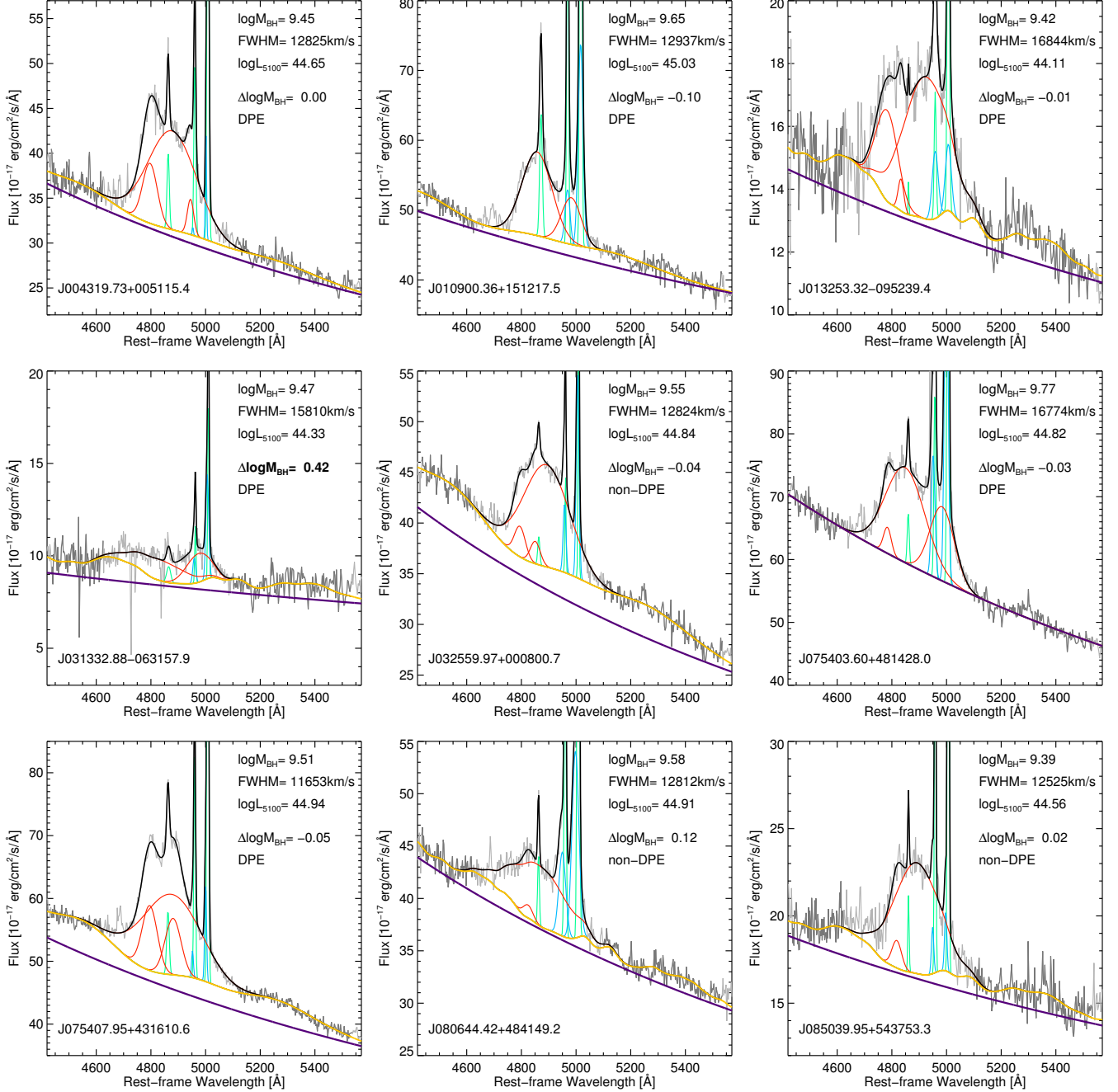
## C. OVERDENSITY MAPS AND CLUSTER MAPS AROUND EXTREMELY MASSIVE QUASARS

In Figure 25, we show large-scale overdensity maps for 52 massive quasars. Details on the description for these figures are given in Section 4.1. In Figure 26, we show maps in which the locations of known clusters are marked for comparison with the overdensity maps in Figure 25. We used the cluster catalog of Wen et al. (2012) for information about the clusters, such as  $M_{200}$  and  $r_{200}$ .<sup>26</sup> In the maps, clusters within  $\Delta z/(1+z) = 0.04$  centered on the redshift of each quasar were used.  $\Delta z/(1+z) = 0.04$  corresponds to the photometric redshift gap used in Wen et al. (2012) to select cluster members. They defined the redshift of each cluster as the median value of photometric redshifts of cluster members.

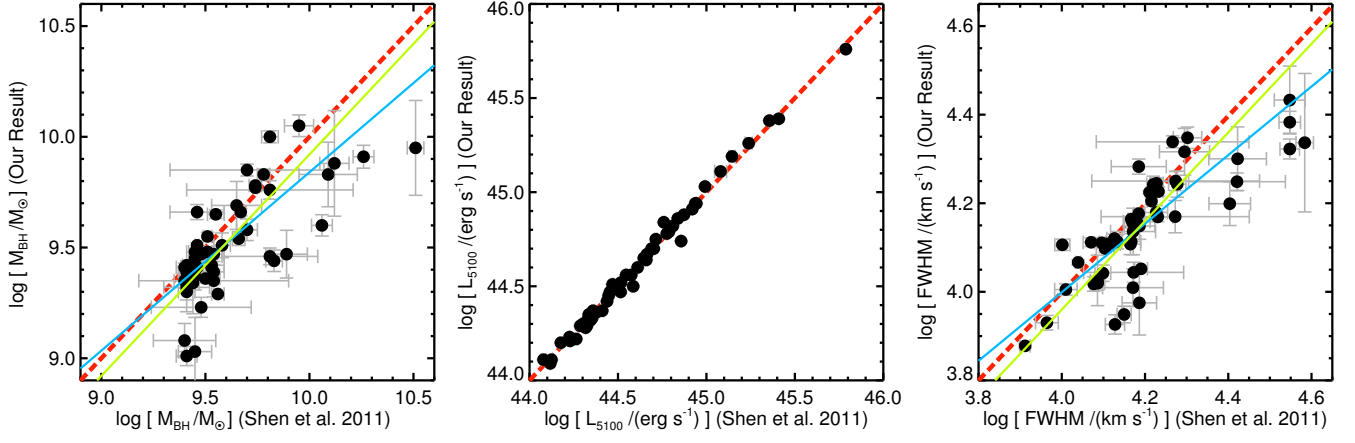
<sup>24</sup> J111724.57+153800.5, J111800.12+233651.5, and J141213.61+021202.1.

<sup>25</sup> Here, we also used the quasars whose uncertainties in logarithmic broad  $H\beta$  line luminosities are less than or equal to 0.05, which corresponds to an S/N higher than  $\sim 8$ .

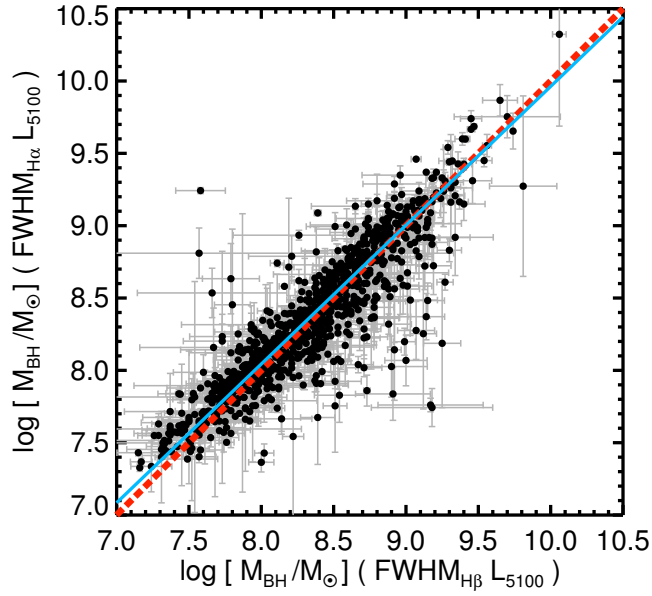
<sup>26</sup>  $r_{200}$  is the radius within which the mean density is 200 times the critical density of the universe.  $M_{200}$  is the cluster mass within  $r_{200}$ .



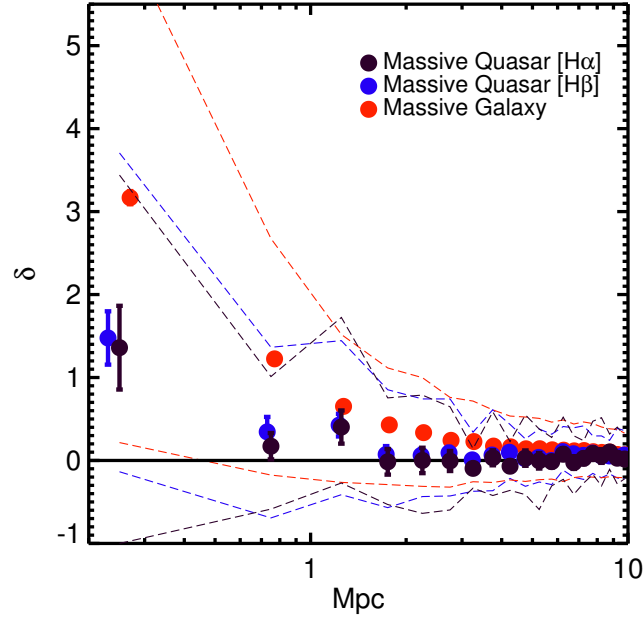
**Figure 19.** Our spectral fitting results for the 52 massive quasars. Also indicated are the best-fit results from our fits and the difference between our and the S11’s BH masses (large differences are written in boldface). We also denote whether the quasar is a DPE or a non-DPE in each panel. The gray line represents the quasar spectrum; the dark gray lines indicate the wavelength windows in which the continuum and iron line template fit was conducted. The purple line indicates the best-fit power-law continuum ( $f_{\lambda} = \alpha\lambda^{\beta}$ ), while the orange line represents the best-fit iron template on the power-law continuum. The green lines are the narrow H $\beta$  line and the core [O III] $\lambda\lambda$ 4959, 5007 lines. The blue lines indicate the blue-wing components for [O III] $\lambda\lambda$ 4959, 5007. The red lines show the multicomponents of the best-fit Gaussian function of the broad H $\beta$  lines. The complete figure set (six images) is available in the online journal.



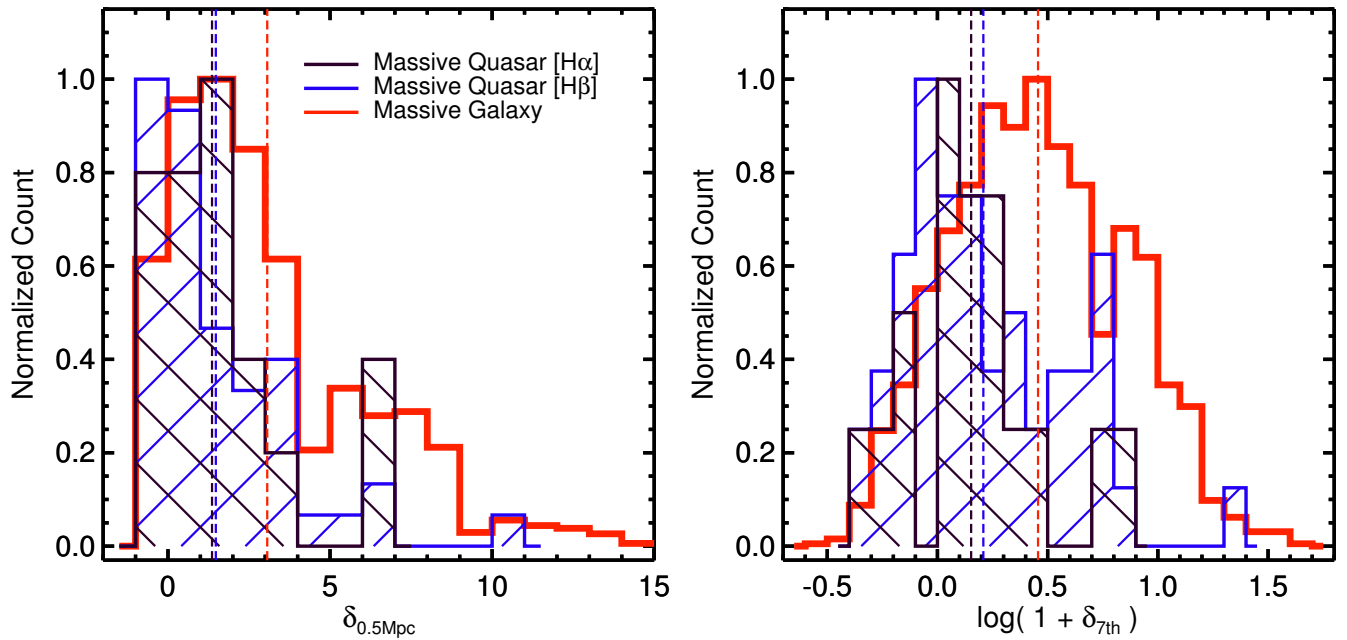
**Figure 20.** Comparison of BH mass (the left panel),  $L_{5100}$  (the middle panel), and FWHM (the right panel) estimates from S11 and our analysis. The blue lines denote the best-fit linear relations fitted with errors in both variables in which the slope is not fixed, while the green lines indicate the best-fit results where the slope is fixed to unity. The red dashed lines indicate the case where the  $x$ -axis and  $y$ -axis values are identical.



**Figure 21.** Comparison between BH masses measured by  $\text{FWHM}_{\text{H}\beta}$  and those measured by  $\text{FWHM}_{\text{H}\alpha}$ . The meanings of the lines are identical to those in Figure 20.

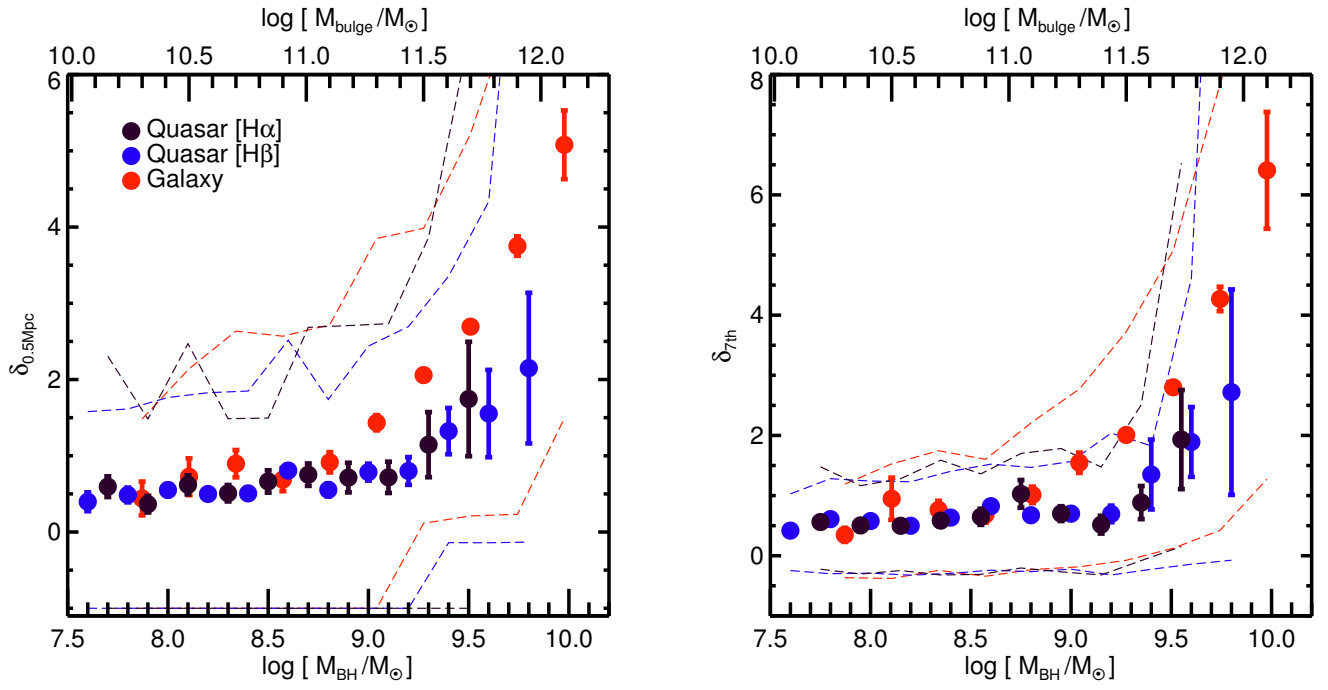


**Figure 22.** Average overdensity as a function of radial distance from the location of massive quasars and massive galaxies. This figure is a counterpart of Figure 9, but we plot here the results based on the  $H\alpha$  and  $H\beta$  analyses at the same time. So, the symbols are the same as those in Figure 9.

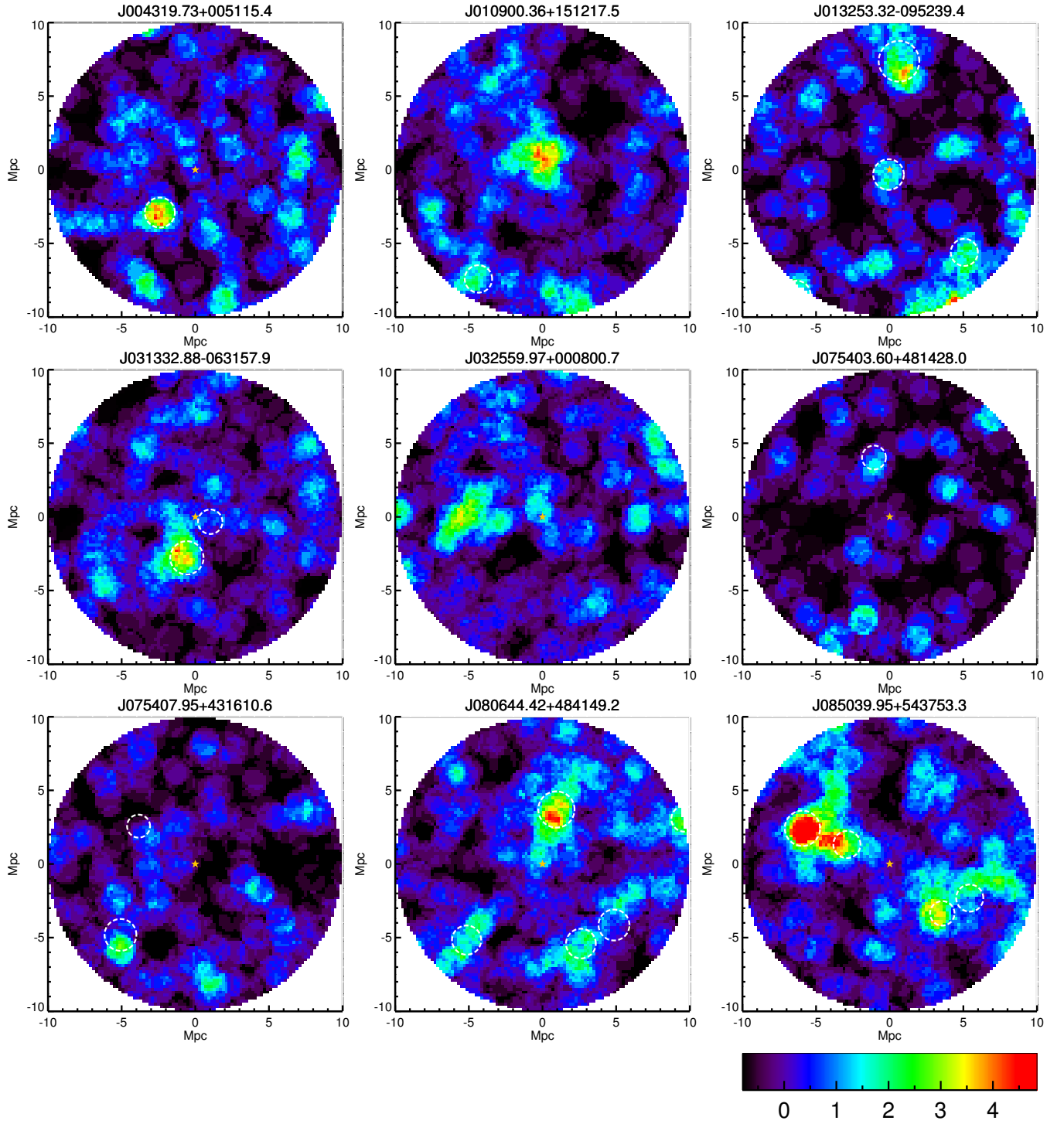


**Figure 23.** Overdensity distributions for environments of massive quasars, with the  $H\alpha$ -based results included. This figure is a counterpart of Figure 10. So, the symbols are the same as those in Figure 10.





**Figure 24.** Mass–overdensity relations, with the  $\text{H}\alpha$ -based results included. This figure is a counterpart of Figure 11. So, the symbols are the same as those in Figure 11.


 $\delta$ 

**Figure 25.** Large-scale overdensity maps over a rectangular area of 20 Mpc in both R.A. ( $x$  axis) and decl. ( $y$  axis) around the 52 massive quasars. The colors represent the color-coded overdensity. The orange stars in the center of the maps are the locations of quasars. The locations of known galaxy clusters are marked as circles. The radius of the circle represents  $r_{200}$  of the cluster. The complete figure set (six images) is available in the online journal.

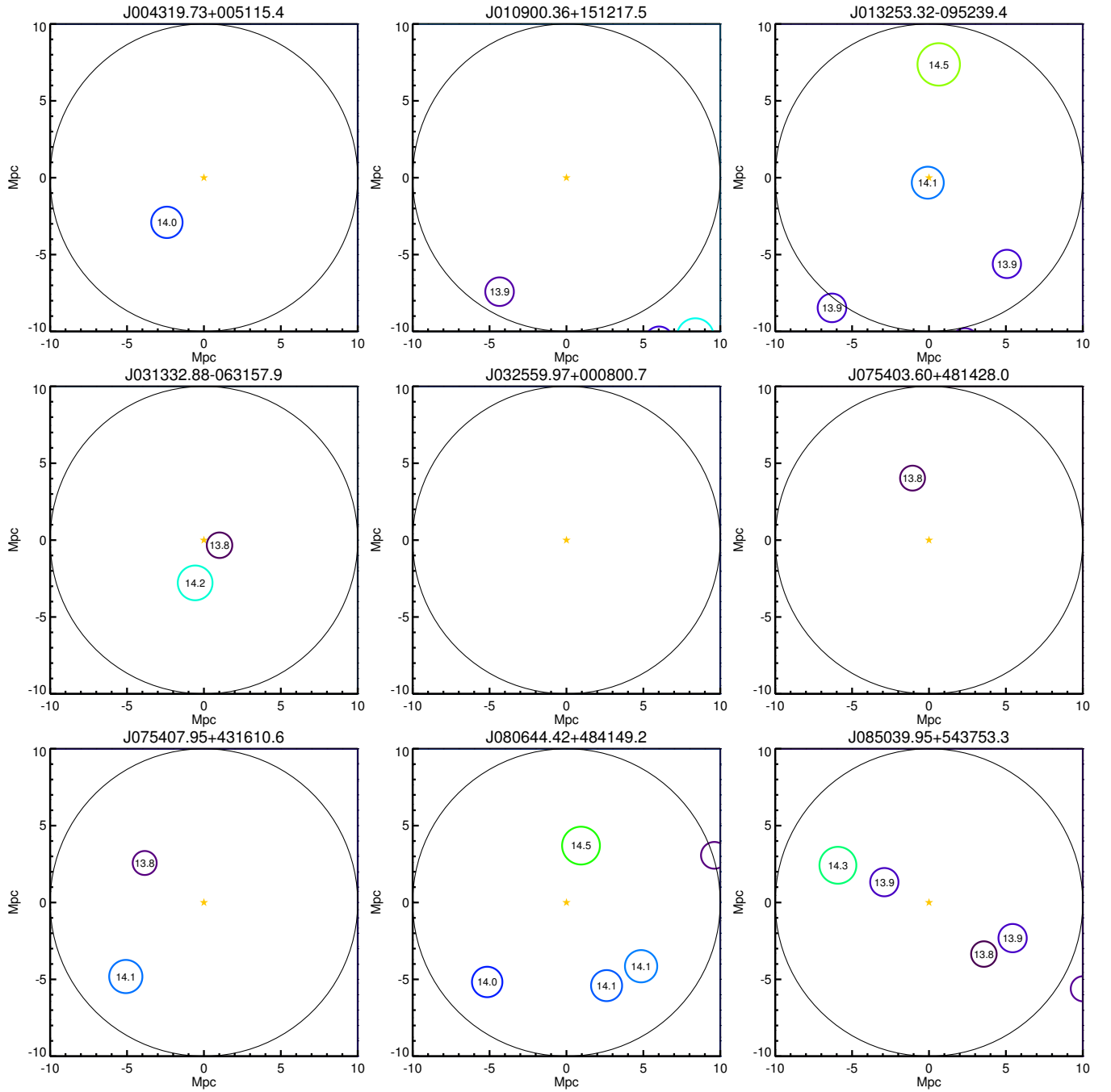


**Figure 26.** Maps in which the locations of known clusters around each quasar are marked as circles. The radius of the circle represents  $r_{200}$  of the cluster, while the color of the circle indicates  $\log(M_{200}/M_{\odot})$ , which is also denoted by the number in the center of the circle. The complete figure set (six images) is available in the online journal.

## REFERENCES

- Abazajian, K. N., Adelman-McCarthy, J. K., Agüeros, M. A., et al. 2009, *ApJS*, 182, 543
- Alam, S., Albareti, F. D., Allende Prieto, C., et al. 2015, *ApJS*, 219, 12
- Bañados, E., Venemans, B., Walter, F., et al. 2013, *ApJ*, 773, 178
- Beck, R., Dobos, L., Budavári, T., Szalay, A. S., & Csabai, I. 2016, *MNRAS*, 460, 1371
- Behroozi, P. S., Conroy, C., & Wechsler, R. H. 2010, *ApJ*, 717, 379
- Bennert, V. N., Auger, M. W., Treu, T., Woo, J.-H., & Malkan, M. A. 2011, *ApJ*, 742, 107
- Bennert, V. N., Treu, T., Woo, J.-H., et al. 2010, *ApJ*, 708, 1507
- Bernardi, M., Meert, A., Vikram, V., et al. 2014, *MNRAS*, 443, 874
- Blanton, M. R., Hogg, D. W., Bahcall, N. A., et al. 2003, *ApJ*, 592, 819
- Boroson, T. A., & Green, R. F. 1992, *ApJS*, 80, 109
- Calzetti, D., Armus, L., Bohlin, R. C., et al. 2000, *ApJ*, 533, 682
- Canalizo, G., & Stockton, A. 2001, *ApJ*, 555, 719
- Catinella, B., Schiminovich, D., Cortese, L., et al. 2013, *MNRAS*, 436, 34
- Chabrier, G. 2003, *PASP*, 115, 763
- Chen, K., Halpern, J. P., & Filippenko, A. V. 1989, *ApJ*, 339, 742
- Coil, A. L., Hennawi, J. F., Newman, J. A., Cooper, M. C., & Davis, M. 2007, *ApJ*, 654, 115
- Coil, A. L., Newman, J. A., Cooper, M. C., et al. 2006, *ApJ*, 644, 671
- Coldwell, G. V., & Lambas, D. G. 2006, *MNRAS*, 371, 786
- Cole, S., Lacey, C. G., Baugh, C. M., & Frenk, C. S. 2000, *MNRAS*, 319, 168
- Conroy, C., Gunn, J. E., & White, M. 2009, *ApJ*, 699, 486
- Croton, D. J., Springel, V., White, S. D. M., et al. 2006, *MNRAS*, 365, 11
- Davies, R. D., & Lewis, B. M. 1973, *MNRAS*, 165, 231
- Decarli, R., Falomo, R., Treves, A., et al. 2010, *MNRAS*, 402, 2453
- Delvecchio, I., Gruppioni, C., Pozzi, F., et al. 2014, *MNRAS*, 439, 2736
- Eisenstein, D. J., Blanton, M., Zehavi, I., et al. 2005, *ApJ*, 619, 178
- Eracleous, M., & Halpern, J. P. 1994, *ApJS*, 90, 1
- Fabricant, D. G., Kurtz, M. J., Geller, M. J., et al. 2008, *PASP*, 120, 1222
- Fanidakis, N., Baugh, C. M., Benson, A. J., et al. 2011, *MNRAS*, 410, 53
- Fanidakis, N., Baugh, C. M., Benson, A. J., et al. 2012, *MNRAS*, 419, 2797
- Fanidakis, N., Georgakakis, A., Mountrichas, G., et al. 2013a, *MNRAS*, 435, 679
- Fanidakis, N., Macciò, A. V., Baugh, C. M., Lacey, C. G., & Frenk, C. S. 2013b, *MNRAS*, 436, 315
- Fitzpatrick, E. L. 1999, *PASP*, 111, 63
- Fried, J. W. 1998, *A&A*, 331, L73
- Fukugita, M., Hogan, C. J., & Peebles, P. J. E. 1998, *ApJ*, 503, 518
- Gaskell, C. M. 2010, *Nature*, 463, E1
- Greene, J. E., & Ho, L. C. 2005, *ApJ*, 627, 721
- Grossi, M., di Serego Alighieri, S., Giovanardi, C., et al. 2009, *A&A*, 498, 407
- Guo, Q., White, S., Boylan-Kolchin, M., et al. 2011, *MNRAS*, 413, 101
- Hashimoto, Y., & Oemler, A., Jr. 2000, *ApJ*, 530, 652
- Hong, J., Im, M., Kim, M., & Ho, L. C. 2015, *ApJ*, 804, 34
- Hopkins, A. M., & Beacom, J. F. 2006, *ApJ*, 651, 142
- Hopkins, P. F., Hernquist, L., Cox, T. J., & Kereš, D. 2008, *ApJS*, 175, 356-389
- Hopkins, P. F., Richards, G. T., & Hernquist, L. 2007, *ApJ*, 654, 731
- Husband, K., Bremer, M. N., Stanway, E. R., et al. 2013, *MNRAS*, 432, 2869
- Hutchings, J. B., & Neff, S. G. 1991, *AJ*, 101, 2001
- Im, M., Griffiths, R. E., & Ratnatunga, K. U. 1997, *ApJ*, 475, 457
- Jahnke, K., Bongiorno, A., Brusa, M., et al. 2009, *ApJL*, 706, L215
- Jun, H. D., Im, M., Kim, D., & Stern, D. 2017, *ApJ*, 838, 41
- Jun, H. D., Im, M., Lee, H. M., et al. 2015, *ApJ*, 806, 109
- Kang, E., & Im, M. 2015, *Journal of Korean Astronomical Society*, 48, 21
- Karhunen, K., Kotilainen, J. K., Falomo, R., & Bettoni, D. 2014, *MNRAS*, 441, 1802
- Kauffmann, G., & Haehnelt, M. 2000, *MNRAS*, 311, 576
- Kelvin, L. S., Driver, S. P., Robotham, A. S. G., et al. 2014, *MNRAS*, 444, 1647
- Kim, M., Ho, L. C., Peng, C. Y., et al. 2008, *ApJ*, 687, 767
- Kim, M., Ho, L. C., Peng, C. Y., Barth, A. J., & Im, M. 2017, *ApJS*, 232, 21
- Kim, Y., Im, M., Jeon, Y., et al. 2018, *ApJ*, 855, 138
- Kim, J.-W., Im, M., Lee, S.-K., et al. 2016, *ApJL*, 821, L10
- Kim, S., Stiavelli, M., Trenti, M., et al. 2009, *ApJ*, 695, 809
- Kochanek, C. S., Eisenstein, D. J., Cool, R. J., et al. 2012, *ApJS*, 200, 8
- Komiya, Y., Shirasaki, Y., Ohishi, M., & Mizumoto, Y. 2013, *ApJ*, 775, 43

- Komossa, S., Xu, D., Zhou, H., Storch-Bergmann, T., & Binette, L. 2008, *ApJ*, 680, 926-938
- Kormendy, J., & Ho, L. C. 2013, *ARA&A*, 51, 511
- Krolewski, A. G., & Eisenstein, D. J. 2015, *ApJ*, 803, 4
- Krumpe, M., Miyaji, T., Husemann, B., et al. 2015, *ApJ*, 815, 21
- Lagos, C. d. P., Bayet, E., Baugh, C. M., et al. 2012, *MNRAS*, 426, 2142
- Lauer, T. R., Faber, S. M., Richstone, D., et al. 2007, *ApJ*, 662, 808
- Leauthaud, A., Tinker, J., Bundy, K., et al. 2012, *ApJ*, 744, 159
- Lee, S.-K., Im, M., Kim, J.-W., et al. 2015, *ApJ*, 810, 90
- Lietzen, H., Heinämäki, P., Nurmi, P., et al. 2009, *A&A*, 501, 145
- Masters, D., & Capak, P. 2011, *PASP*, 123, 638
- McConnell, N. J., Ma, C.-P., Gebhardt, K., et al. 2011, *Nature*, 480, 215
- McConnell, N. J., & Ma, C.-P. 2013, *ApJ*, 764, 184
- McDonald, M., Bayliss, M., Benson, B. A., et al. 2012, *Nature*, 488, 349
- McDonald, M., Benson, B., Veilleux, S., Bautz, M. W., & Reichardt, C. L. 2013, *ApJL*, 765, L37
- McLure, R. J., Jarvis, M. J., Targett, T. A., Dunlop, J. S., & Best, P. N. 2006, *MNRAS*, 368, 1395
- Merloni, A., Bongiorno, A., Bolzonella, M., et al. 2010, *ApJ*, 708, 137
- Merloni, A., & Heinz, S. 2008, *MNRAS*, 388, 1011
- Mendel, J. T., Simard, L., Palmer, M., Ellison, S. L., & Patton, D. R. 2014, *ApJS*, 210, 3
- Mosleh, M., Williams, R. J., & Franx, M. 2013, *ApJ*, 777, 117
- Muldrew, S. I., Croton, D. J., Skibba, R. A., et al. 2012, *MNRAS*, 419, 2670
- Myers, A. D., Brunner, R. J., Nichol, R. C., et al. 2007, *ApJ*, 658, 85
- Myers, A. D., Richards, G. T., Brunner, R. J., et al. 2008, *ApJ*, 678, 635-646
- Netzer, H. 2003, *ApJL*, 583, L5
- Orsi, Á. A., Fanidakis, N., Lacey, C. G., & Baugh, C. M. 2016, *MNRAS*, 456, 3827
- Planck Collaboration, Ade, P. A. R., Aghanim, N., et al. 2016, *A&A*, 594, A13
- Reynolds, C. S., Lohfink, A. M., Babul, A., et al. 2014, *ApJL*, 792, L41
- Russell, H. R., Fabian, A. C., Sanders, J. S., et al. 2010, *MNRAS*, 402, 1561
- Salviander, S., Shields, G. A., Gebhardt, K., & Bonning, E. W. 2007, *ApJ*, 662, 131
- Schlegel, D. J., Finkbeiner, D. P., & Davis, M. 1998, *ApJ*, 500, 525
- Shankar, F., Weinberg, D. H., & Miralda-Escudé, J. 2009, *ApJ*, 690, 20
- Shen, Y., & Loeb, A. 2010, *ApJ*, 725, 249
- Shen, Y., & Liu, X. 2012, *ApJ*, 753, 125
- Shen, Y., McBride, C. K., White, M., et al. 2013, *ApJ*, 778, 98
- Shen, Y., Richards, G. T., Strauss, M. A., et al. 2011, *ApJS*, 194, 45
- Shen, Y., Strauss, M. A., Ross, N. P., et al. 2009, *ApJ*, 697, 1656
- Shields, G. A., Menezes, K. L., Massart, C. A., & Vanden Bout, P. 2006, *ApJ*, 641, 683
- Shirasaki, Y., Komiya, Y., Ohishi, M., & Mizumoto, Y. 2016, *PASJ*, 68, 23
- Shim, H., Im, M., Ko, J., et al. 2013, *ApJS*, 207, 37
- Simard, L., Mendel, J. T., Patton, D. R., Ellison, S. L., & McConnachie, A. W. 2011, *ApJS*, 196, 11
- Simpson, C., Mortlock, D., Warren, S., et al. 2014, *MNRAS*, 442, 3454
- Söchting, I. K., Clowes, R. G., & Campusano, L. E. 2002, *MNRAS*, 331, 569
- Söchting, I. K., Clowes, R. G., & Campusano, L. E. 2004, *MNRAS*, 347, 1241
- Solanes, J. M., Manrique, A., García-Gómez, C., et al. 2001, *ApJ*, 548, 97
- Song, H., Park, C., Lietzen, H., & Einasto, M. 2016, *ApJ*, 827, 104
- Springel, V., White, S. D. M., Jenkins, A., et al. 2005, *Nature*, 435, 629
- Strateva, I. V., Strauss, M. A., Hao, L., et al. 2003, *AJ*, 126, 1720
- Strazzullo, V., Gobat, R., Daddi, E., et al. 2013, *ApJ*, 772, 118
- Trainor, R. F., & Steidel, C. C. 2012, *ApJ*, 752, 39
- Treu, T., Malkan, M. A., & Blandford, R. D. 2004, *ApJL*, 615, L97
- Treu, T., Woo, J.-H., Malkan, M. A., & Blandford, R. D. 2007, *ApJ*, 667, 117
- Uchiyama, H., Toshikawa, J., Kashikawa, N., et al. 2018, *PASJ*, 70, S32
- van den Bosch, R. C. E., Gebhardt, K., Gültekin, K., et al. 2012, *Nature*, 491, 729
- van Dokkum, P. G., Whitaker, K. E., Brammer, G., et al. 2010, *ApJ*, 709, 1018
- Vestergaard, M., Fan, X., Tremonti, C. A., Osmer, P. S., & Richards, G. T. 2008, *ApJL*, 674, L1
- Vestergaard, M., & Peterson, B. M. 2006, *ApJ*, 641, 689

- Walker, S. A., Fabian, A. C., Russell, H. R., & Sanders, J. S. 2014, *MNRAS*, 442, 2809
- Wang, Y., Brunner, R. J., & Dolence, J. C. 2013, *MNRAS*, 432, 1961
- Wen, Z. L., & Han, J. L. 2011, *ApJ*, 734, 68
- Wen, Z. L., Han, J. L., & Liu, F. S. 2012, *ApJS*, 199, 34
- Wold, M., Lacy, M., Lilje, P. B., & Serjeant, S. 2001, *MNRAS*, 323, 231
- Woo, J.-H., Schulze, A., Park, D., et al. 2013, *ApJ*, 772, 49
- Woo, J.-H., Treu, T., Barth, A. J., et al. 2010, *ApJ*, 716, 269
- Woo, J.-H., Treu, T., Malkan, M. A., & Blandford, R. D. 2006, *ApJ*, 645, 900
- Woo, J.-H., Treu, T., Malkan, M. A., & Blandford, R. D. 2008, *ApJ*, 681, 925
- Wu, X.-B., Wang, F., Fan, X., et al. 2015, *Nature*, 518, 512
- Yang, X., Mo, H. J., van den Bosch, F. C., Zhang, Y., & Han, J. 2012, *ApJ*, 752, 41
- Yi, S. K., Lee, J., Jung, I., Ji, I., & Sheen, Y.-K. 2013, *A&A*, 554, A122
- Yoon, Y., Im, M., & Kim, J.-W. 2017, *ApJ*, 834, 73
- Zehavi, I., Zheng, Z., Weinberg, D. H., et al. 2005, *ApJ*, 630, 1
- Zhang, X.-G., Dultzin-Hacyan, D., & Wang, T.-G. 2007, *MNRAS*, 376, 1335
- Zhang, S., Wang, T., Wang, H., & Zhou, H. 2013, *ApJ*, 773, 175